STUDY OF THE ROLE OF CCAP NEURONS IN THE CONTROL OF THE ECDYSIAL BEHAVIORAL SEQUENCE THROUGH MATHEMATICAL AND COMPUTATIONAL METHODS

Tesis entregada a

LA UNIVERSIDAD DE VALPARAÍSO

en Cumplimiento Parcial de los requisitos para optar al grado de

Doctor en Ciencias con Mención en Neurociencias

Facultad De Ciencias

Por

Miguel Piñeiro Feick

Mayo, 2018

Dirigida por: Patricio Orio Alvarez

FACULTAD DE CIENCIAS

UNIVERSIDAD DE VALPARAÍSO

INFORME DE APROBACION

TESIS DE DOCTORADO

Se informa a la Facultad de Ciencias que la Tesis de Doctorado presentada por:

Miguel Piñeiro Feick

Ha sido aprobada por la comisión de Evaluación de la tesis como requisito para optar al grado de Doctor en Ciencias con mención en Neurociencia, en el examen de Defensa de Tesis rendido el día (día) del mes de (mes) de (año).

Director/a de Tesis:

Dr. Patricio Orio Alvarez _____

Presidente:

Dr. Adrian Palacios Vargas _____

Comisión de Evaluación de la Tesis:

Dr. John Ewer Lothian _____

Dr. Tomas Perez Acle _____

Dr. Rodrigo Salas Fuentes _____

To Wilhelm Feick Lehfeldt,

who inspired me to follow a career in engineering and science

and whose role in my life was, and remains, immense.

Acknowledgements

First and foremost, I would like to express my most sincere gratitude to my advisor Patricio Orio for his continuous support and guidance through all these years. I am also in debt to the members of the committee, Adrian Palacios, John Ewer, Tomas Perez-Acle and Rodrigo Salas, for their insightful comments and invaluable feedback. I'm very thankful to Wilson Mena for introducing me to the study of ecdysis and supplying me with the experimental data used in this study.

I would like to thank the professors of the program for their teachings; and the program for providing me the opportunity to do this study. I'm also grateful to the members of the laboratory for their useful advice, feedback, on and of course friendship.

I am thankful for the access to high performance computational resources provided by Patricio Orio's laboratory, and the National Laboratory for High Performance Computing (NLHPC). This study would not have been possible without the financial support of Fondo Institucional de Becas Universidad de Valparaiso (FIB-UV), Anillo ACT-1113, and Centro Interdisciplinario de Neurociencia Valparaiso (CINV).

I am profoundly grateful to Antonio Glaria for introducing me to the exciting world of artificial neural networks and convincing to pursue a graduate degree (which I'm glad I did).

Finally, heartfelt thanks go to my parents, life partner and friends for their unconditional support and encouragement over the years and especially during my doctoral journey.

Table of contents

List of Figures

List of Tables

Abbreviations

2D two dimensions.

AIC akaike information criterion.

AP action potential.

AUC area under the curve.

BURS bursicon.

CCAP crustacean cardioactive peptide.

CCAP-R CCAP receptor.

CER classification error rate.

CNS central nervous system.

CPG central pattern generator.

CWT continuous wavelet transform.

EH eclosion hormone.

ETH ecdysis-triggering hormone.

ETHR ETH receptor.

ETHR-A ETH receptor A isoform.

ETHR-B ETH receptor B isoform.

FMRF FMRFamide.

FN false negative.

FP false positive.

FPR false positive rate.

GABA γ-aminobutyric acid.

GABA-RA $GABA_A$ receptor.

GFP green fluorescent protein.

GPCR G protein-coupled receptor.

ISI interspike interval.

LDCV large dense core vesicle.

MIP myoinhibitory peptide.

MLE maximum likelihood estimation.

PBURS partner of bursicon.

PDF probability distribution function.

RGB red green blue.

RNAi RNA interference.

ROC receiver operating characteristic.

ROI region of interest.

SEM standard error of the mean.

SNR signal to noise ratio.

STFT short-time Fourier transform.

STG stomatogastric ganglion.

TPR true positive rate.

Abstract

Animal behavior arises from the interplay between neural, biomechanical and environmental dynamics. Neuromodulators, such as neuropeptides can regulate and reconfigure neural circuits to alter their output, affecting in this way animal behavior. How neuromodulators act on neural circuits to produce distinct behaviors is still poorly understood. Here I studied the peptidergic circuits that orchestrates the ecdysis behavioral sequence in *Drosophila*. This behavioral sequence has three phases: pre-ecdysis, ecdysis and post-ecdysis. The sequence is initiated by the release of ecdysis-triggering hormone (ETH) which activates multiple neuronal targets of which crustacean cardioactive peptide (CCAP) neurons have been identified as key for the successful execution of the behavioral sequence. How CCAP neurons regulate the behavioral sequence is still not clear, but studies of *Manduca* have showed that CCAP can initiate the ecdysial motor activity. I used calcium imaging data (from CCAP neurons only, and from CCAP neurons together with motoneurons), behavioral data from pupal ecdysis, and mathematical and computational approaches to study the dynamics and functional connectivity between CCAP neurons and motoneurons, and how they relate to the behavior. I found that CCAP neurons tightly regulate the motoneuronal activity during the ecdysis and post-ecdysis phases, consistent with the recent identification of CCAP targets. The behavioral analysis showed that while the three major phases of the ecdysis sequence can be detected in the motoneuronal recordings, motoneurons have major differences in the timing and regularity of their activity. Moreover, I found that the post-ecdysis phase has two subphases which appear to be absent in the motoneuronal recordings. These results give us new insights into the peptidergic regulation of motor programs and behaviors.

1 Introduction

1.1 Behavior

Behavior has been defined as the coordinated responses of organisms to internal or external stimuli (Levitis et al. 2009). Its importance for the fitness and survival of animals was recognized early on by Darwin who proposed that instincts were selected through evolution (Darwin 1859).

In a narrower scope Gomez-Marin et al. 2014 stated that animal behavior is the muscular response of an organism. Furthermore, he stated that it is the unifying organismal process where genes, neural function, anatomy and environment converge and interrelate.

He highlighted three important attributes of animal behavior. It is relational, and its study requires us to consider the environment context. It is dynamic and is manifested in space and time, and best studied through time series analyses. And it is high dimensional, as it manifests itself in multiple simultaneous outputs; making dimensionality reduction an important technique to make the study tractable.

Traditionally animal behavior has been the subject of study of ethology, founded by Nikolaas Tinbergen, Konrad Lorentz and Karl Von-Frisch in the middle of the 20th century (Anderson and Perona 2014; Zilkha et al. 2016; Zupanc 2010). Ethology studies behavior of animals in their natural habitat, or laboratory conditions close to their natural environment, avoiding any artificial disturbances as much as possible (Gomez-Marin et al. 2014; Zilkha et al. 2016; Zupanc 2010).

Naturally, there was interest in the study of how the nervous system orchestrates behaviors, this led to the birth of a new discipline, neuroethology (Zilkha et al. 2016; Zupanc 2010). Neuroethology, in opposition to classical neurobiology, studies behavior as it would occur in an animal's natural environment; and in opposition to classical ethology, focuses on simple behaviors, such as rhythmic movements.

The study of simple behaviors has provided neuroethologists valuable insights into important neurobiological phenomena, such as central pattern generators (CPGs) [1] and neuromodulation [2] (Zupanc 2010). Through the study of the crustacean stomatogastric ganglion (STG) for example, it has been shown that CPGs can be reconfigured through multiple neuromodulatory substances to output different rhythmic motor patterns (Marder and Bucher 2007; Stein 2009).

[1] CPGs are neural circuits capable of producing a rhythmic output in absence of rhythmic input.

[2] Neuromodulation is the process by which neurons release diffusible substances (neuromodulators) that act on nearby cells, usually by reconfiguring their mode of operation.

How neuromodulators act on CPGs to alter the behavioral output of the animal, is a major question of neuroethology and neuroscience (Dickinson 2006; Marder 2012; Nusbaum and Blitz 2012; Zupanc 2010).

One relevant behavior to study the interplay between neuromodulators, CPGs and behavior, is the ecdysis behavioral sequence. As arthropods go through multiple developmental stages, they perform a stereotyped behavioral sequence known as ecdysis, where the old cuticle is first loosened and shed, and then the new cuticle expands and hardens, allowing the animal to continue growing (Reynolds 1980).

In *Drosophila*, multiple neuropeptides have been implicated in the regulation of the ecdysis sequence, but their precise role is still poorly understood (Mena et al. 2016). Moreover, we still do not know the number of CPGs involved in the production of the behaviors, their structure and their regulatory mechanisms.

1.2 Central pattern generators

CPGs have been defined as neural circuits that generate rhythmic patterned outputs in the absence of rhythmic sensory input (Hooper 2000; Marder and Bucher 2001). Before their discovery, it was thought that rhythmic behaviors were produced by reflex activation, later it was demonstrated that deafferented locusts could generate rhythmic flight behavior in response to non-rhythmic stimulation of the nerve cord (Marder and Bucher 2001; Marder and Calabrese 1996; Selverston 2010). Subsequent studies showed similar results in a wide variety of animals, where oscillatory activity was generated in the absence of sensory feedback (Marder and Bucher 2001).

CPGs underlie a large variety of behaviors that include stereotyped movements such as breathing, chewing, walking, flying, swimming, eclosion, intestinal movements and heartbeat, among others (Delcomyn 1980; Hooper 2000; Marder and Calabrese 1996). Some of these behaviors are ongoing (as in breath or heartbeat behaviors), some are rare (as in escape or scratch behaviors), some occur during development (as in hatching or ecdysis behaviors), while others can occur for short or long periods of time (as in locomotion behaviors) (Marder and Calabrese 1996). CPGs do not necessarily operate ballistically, they can indeed be regulated by synaptic input and sensory feedback (as in the walking of the stick insect) and through neuromodulatory action (as in the STG) (Marder and Bucher 2001). In the stick insect walking requires the coordination between adjacent leg joints within one leg and between different legs; the coordination between different joints is then achieved by a combination of CPG

synaptic coupling and sensory feedback (Marder and Bucher 2001). In the *Cancer irroratus* crab, the neuropeptide proctolin can modify the motor pattern produced by the STG.

The rhythmic activity of CPGs arises either through interactions among currents in individual neurons (endogenous oscillator) or through interactions among neurons (network-based rhythmicity) (Hooper 2000; Marder and Bucher 2001). In an endogenously oscillating (also called pacemaking) driven network, a neuron drives neurons that are not themselves bursting, into rhythmic activity, as in the case of the pyloric rhythm of the crustacean STG (Hooper 2000; Marder and Bucher 2001). Network-based rhythmicity (also called half-center oscillators) networks consists of two neurons that individually have no rhythmogenic ability, but which produce rhythmic activity when reciprocally coupled (Hooper 2000; Marder and Bucher 2001), as occurs in the leech heartbeat network (Hooper 2000).

One key component that adds tremendous richness to the dynamics of CPGs are neuropeptides, which differ in many relevant aspects from conventional neurotransmitters (Bargmann 2012; Brezina 2010; Dickinson 2006; Marder 2011, 2012; Nusbaum and Blitz 2012).

1.3 Neuropetides

Conventional neurotransmitters are packed in small vesicles, released from axonal terminals into the synaptic cleft and act with half-lives of $\sim$5 ms, and are constrained spatio-temporally by efficient reuptake mechanisms (Zhang et al. 2010). In contrast, neuropeptides are packed in large dense core vesicles (LDCVs) that can be released along axons, cell bodies, and even at dendrites; they act with orders of magnitude longer half-lives, which allows them to diffuse greater distances (Nusbaum and Blitz 2012; Zhang et al. 2010). As neuropeptides can act on more distant receptors, they tend to have higher affinity, and are usually coupled to intracellular second messenger pathways that amplify the signal (Zhang et al. 2010). Neuropeptides can act in an autocrine manner, as a form of feedback mechanism, in a paracrine manner, on close targets, or in a neurohormonal manner, on distant targets (Nusbaum and Blitz 2012; Zhang et al. 2010). Neuropeptides usually exert their action through G protein-coupled receptors (GPCRs), and can therefore reconfigure neural circuits by causing relatively long-lasting effects on the circuit dynamics (Bargmann 2012; Nusbaum and Blitz 2012; Zhang et al. 2010).

A major question in neuroscience has been how neuromodulators act on neural circuits to produce distinct output patterns (Bargmann 2012; Brezina 2010; Dickinson 2006; Marder 2012; Nässel and Winther 2010; Nusbaum and Blitz 2012).

1.4 *Drosophila melanogaster* ecdysis behavioral sequence

The fruit fly *Drosophila melanogaster* is an important model system for the study of the molecular and genetic bases of complex behaviors (Griffith 2012). The fly is suitable for the study of mechanisms underlying behavior at the level of genes, neurons and circuits, as its neurons are identifiable and genetically tractable (Kazama 2015). Its rich behavioral repertoire, the increasingly sophisticated methods of manipulation and recording of its nervous system have made the fly an attractive system to explore the neural circuits that underlie behavior (Griffith 2012; Kazama 2015).

In this thesis I studied the ecdysis to the pupa of the *Drosophila melanogaster* to better understand how peptidergic circuits operate to give rise to the ecdysis behavioral sequence.

At the end of its larval stage, *Drosophila* enters the prepupal stage, ecdyses to the pupa and finally undergoes metamorphosis to the adult (Lahr et al. 2012). The pupal ecdysis sequence can be divided into three behavior phases (Kim et al. 2006; Park et al. 2003):

1. The pre-ecdysis phase features anteriorly directed rhythmic peristaltic contractions, alternating on the left and right side of the animal, causing the separation of the pupal cuticle from the puparium.

2. The ecdysis phase presents lateral swinging contractions, alternating between the left and right side of the pupa, and result in the animal head eversion.

3. The post-ecdysis phase is characterized by the alternation between swinging and anteroposterior stretch-compression behaviors.

The ecdysis sequence begins with the release of ETH by the Inka cells, found on the trachea of *Drosophila* and many other insects (Zitnan 2003). Its release stimulates a pair of brain neurons to release the neuropeptide eclosion hormone (EH), which in turn increases the release of ETH by the Inka cells, forming a positive-feedback loop (Ewer et al. 1997; Kingan et al. 1997). The fruit fly genome encodes two ETH receptor (ETHR) isoforms, ETHR-A and ETHR-B, via alternative splicing (Kim et al. 2006). The two isoforms are expressed in different neuron populations (Diao et al. 2016; Kim et al. 2006). ETHR-A neurons have been found to also express the neuropeptides FMRFamide (FMRF), Kinin, EH, CCAP, myoinhibitory peptides (MIPs) and the heterodimer Bursicon (made of bursicon (BURS) and partner of bursicon (PBURS) subunits) (Kim et al. 2006; Lahr et al. 2012).

The release of ETH sequentially activates different ETHR neurons (Kim et al. 2015; Kim et al. 2006; Mena et al. 2016). Within the ETHR-A expressing cells, the CCAP neurons from the AN1-AN4 abdominal segments, which also express the heterodimeric neurohormone Bursicon, have been

identified as critical for the generation of the ecdysis motor pattern (Diao et al. 2017; Kim et al. 2015; Lahr et al. 2012; Mena et al. 2016). The CCAP neurons can be divided into two groups, α and β neurons, which produce different activity patterns (Mena et al. 2016). α and β neurons are located laterally and medially respectively, with each segment having 2 neurons of each type (Kim et al. 2015; Kim et al. 2006; Mena et al. 2016).

It has been shown in *Manduca sexta* that CCAP can turn on the ecdysial motor pattern (Gammie and Truman 1997), but it is not clear if this would still occur in *Drosophila*. Non-simultaneous recordings of CCAP neurons and motoneurons in *Drosophila* appear to show a temporal match of the onset of their increased activity, and its duration (Mena et al. 2016). Mutants that lack PBURS have difficulty executing the ecdysis behavior and pharate adults display severe defects in the head, legs and wings (Lahr et al. 2012). ETH RNAi targeted at CCAP neurons cause severe defects in the ecdysis behavior (Kim et al. 2015; Mena et al. 2016). $GABA_A$ receptor (GABA-RA) RNAi directed at the CCAP neurons considerably shorten the pre-ecdysis phase, pointing again the importance of these neurons in the coordination of the ecdysis motor patterns.

So far ecdysis has been studied mostly through the disruption of its regulatory system by different means, such as genetic, pharmacologic or mechanical methods, and the observation and analysis of resulting changes in the neural activity, behavior or development (Arakane et al. 2008; Baker et al. 1999; Carlson and Bentley 1977; Diao et al. 2017, 2016; Ewer et al. 1997; Gammie and Truman 1997; Kim et al. 2015; Kim et al. 2006; Lahr et al. 2012; Mena et al. 2016; Park et al. 2003; Park et al. 2002). The analyses have usually been statistical analyses of direct measurements, such as the onset time, the duration, or the amplitude of the response. As some features of the experimental data may be hard to quantify, such as cross-frequency neuronal coupling (Hya et al. 2015) or behavioral patterns, researchers may not be able to draw accurate conclusions from the data in those cases. Computational methods on the other hand can detect subtle features in the data that may go unnoticed to visual inspection or simpler analytic methods.

I studied the neural activity of CCAP neurons and motoneurons and the behavior during the ecdysis sequence in *Drosophila melanogaster*. I also used simultaneous calcium imaging of CCAP neurons and motoneurons, and through mathematics, computational methods and models, I characterized their activity patterns and their functional connectivity. Finally, I characterized the behavior activity patterns of the puparium-free preparations and contrasted them to the motoneuronal calcium activity.

I developed multiple techniques and computational algorithms such as a stabilization algorithm, two neuronal models, and a pupal oscillation analysis algorithm. As these mathematical and computational methods have not been used before in the study of the ecdysis sequence, they allowed me to analyze it from a different perspective.

I found that α AN1-AN4 CCAP neurons are functionally tightly coupled to the motoneurons during the ecdysis and post-ecdysis phase in a cross-frequency manner. This allowed me to fit a probabilistic logistic model to the experimental data, to predict the moments where motoneurons had a high chance of oscillating. I also developed a conductance-based model able to simulate many of the observed features of the experimental data. Finally, behavioral analyses showed critical differences between *in vivo* and *ex vivo* preparations, such as the existence of two subphases of post-ecdysis.

1.4.1 General objective

To characterize the activity patterns of CCAP neurons, motoneurons, and pupal movements during the ecdysis sequence using mathematical and computational tools to find how these elements are functionally coupled.

1.4.2 Specific objectives

- Characterize the activity of CCAP neurons and motoneurons in the time and time-frequency domain.
- Characterize their functional connectivity using statistical methods and build a model that can predict the motoneuronal activity out of the CCAP neuron activity.
- Characterize the pupal behavior patterns through machine vision algorithms and compare them to the motoneuronal activity patterns.

2 Methods

2.1 Experimental data

Experimental data were recorded and provided by Wilson Mena and consisted of 7 CCAP neurons calcium imaging recordings, 9 CCAP neurons + motoneurons calcium imaging recordings, and 6 recordings of puparium-free preparations. Different video resolutions, number of z-stack layers, frame rates and video durations were used, as shown in Table 1.

Experimental data	n	Resolution (pixels)	Layers	Frame rate (fps)	Duration (min)
CCAP neurons	4	1344x1024	1	1/5	60
”	3	1376x1038	1	1/5	60
CCAP neurons and Motoneurons	7	1344x1024	5	1/3	60
”	2	1344x1024	3	1/2	60
Puparium-free preparation	1	640x480	1	3	33
”	1	640x480	1	3	57
”	1	640x480	1	3	65
”	1	640x480	1	3	66
”	1	640x480	1	3	71
”	1	640x480	1	3	73

Table 1. Experimental data.

For calcium imaging, the CNS of the prepupa was extracted, stimulated with synthetic ETH and its green fluorescent protein (GFP) fluorescence captured. The genetically encoded calcium sensitive GFP, GCaMP, was used as calcium sensor, and expressed only in the target cells.

For the behavioral recordings, after the detection of the first signs of onset of the behavioral sequence, the pupa was surgically removed from the puparium and recorded.

Experimental protocols are described in detail in Mena et al. 2016

2.2 Image stabilization

As I did not want the neurons to move away from the regions of interest I developed an image stabilization algorithm that does not cause any noticeable drift of neurons, and is not affected by the duration of the video or the oscillating neuronal “glow”. The algorithm iteratively transforms each image of the video sequence so that it better matches the rest of the images of the video. The process is repeated until no further transformations can improve the matching. The transformations used were geometrical translations, and the distance function used was the Pearson’s correlation.

The algorithm proved to be effective at stabilizing the images and had important advantages over the image stabilization ImageJ plugin (Li 2008; Rasband 2013). The fitting of each frame to the rest of the frames had the effect of completely removing any drift no matter the duration of the video, as opposed to algorithms where only consecutive images are compared and fitted. Also, the Pearson's correlation coefficient proved to be a robust distance function, immune to variations in the intensity of the GCaMP signal. Figure 1 shows an example of the ability of the algorithm to stabilize a single neuron.

The pseudo-code of the algorithm is:

```
for block in blockArray:
    do:
        for target in frameArray:
            bestDistance = infinity

            for transformation in transformationArray:
                distance = 0

                for i in frameArray:
                    if target != i:
                        transformedBlock = transform(block[i], transformation)
                        distance += blockDistance(block[target], transformedBlock)

                if bestDistance > distance:
                    bestDistance = distance
                    bestTransformation = transformation

            bestTransformationArray[target] = bestTransformation

        loop = True

        for target in frameArray:
            block[target] = transform(block[target], bestTransformationArray[target])

            if bestTransformationArray[target] != nulTransformation:
                loop = False

    while loop
```

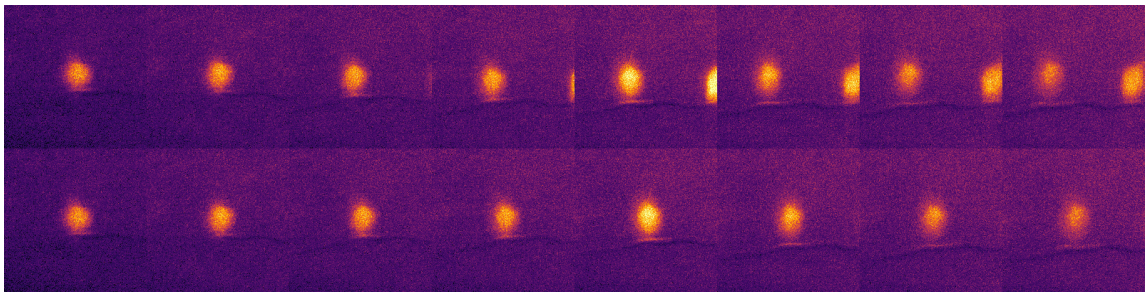

Figure 1. Image stabilization. Drifting of a single CCAP neuron during a 1 h of video recording shown in 8 equally time-spaced images. Top shows the unprocessed video and bottom the output of the stabilization algorithm.

2.3 Time series preprocessing

Calcium time series were preprocessed through detrending and normalization. Detrending was applied to compensate for slow variations of fluorescence during the recording caused by noise, while normalization was applied to make time series more uniforms in terms of the minimum and maximum fluorescence.

Detrending was performed by subtracting a line that passes between the minimum of the first and the last 250 s of the signal, to the signal. The normalization linearly transformed the signal to set its lowest value to 0 and its highest to 1. Mathematically, the preprocessing can be expressed as:

$$\exists t_0 \in [0, 250] \mid f(t_0) = \min_{t \in [0,250]} f(t) \tag{1a}$$

$$\exists t_1 \in [3350, 3600] \mid f(t_1) = \min_{t \in [3350,3600]} f(t) \tag{1b}$$

$$m = \frac{f(t_1) - f(t_0)}{t_1 - t_0} \tag{1c}$$

$$g(t) = f(t) - mt \tag{1d}$$

$$f_{\text{min}} = \min_{t \in [0,3600]} g(t) \tag{1e}$$

$$f_{\text{max}} = \max_{t \in [0,3600]} g(t) \tag{1f}$$

$$h(t) = \frac{g(t) - f_{\text{min}}}{f_{\text{max}} - f_{\text{min}}} \tag{1g}$$

Where $f(t)$, $g(t)$, $h(t)$ are the unprocessed, the detrended and the preprocessed signals. t_0, t_1 are the time of the minimum value within the first and last 250 s of the signal respectively, and m the slope

of the detrending line. f_{min} and f_{max} are the minimum and maximum value of the detrended signal. The value of 250 s was chosen because it produced good results at finding the basal fluorescence at the beginning and end of the time series.

2.4 Activity onset computation

The computation of α CCAP neurons and motoneurons activity onset was performed as follows:

1. The first 100 s of the time series were discarded because some neurons displayed a high level of fluorescence at the beginning of the recordings.
2. A new time series was generated by convolving the original time series with a rectangular window function of 10 s of duration and area of 1.
3. The onset was defined to be first instant where convolved time series exceeded 1/2 of the maximum amplitude of the original time series.

I selected this method over the usual deviation from the mean by a defined amount of standard deviations because this method produced more consistent results. The reason is that in most time series the fluorescence "drifted" slowly during the pre-ecdysis phase, and this had a great impact on the mean and standard deviation, making the method unreliable.

The rectangular window size was chosen so that it acted as a low pass filter in order to avoid false positives and at the same time not miss the onset.

2.5 Time-frequency analysis

The continuous wavelet transform (CWT) can locate frequency components in time, similar to the short-time Fourier transform (STFT). The STFT is a Fourier transform applied to a small fixed-size window, with the drawback of having time and frequency resolution that depend on the size of the window. The CWT on the other hand uses a varying window size, and as result higher frequency signal components can be detected at higher temporal resolution. Also, while the STFT can be seen as a convolution between a signal and a complex exponential, the CWT is a convolution between a signal and an arbitrary wavelet function. The CWT is defined as:

$$W(t,s) = \frac{1}{s}\int_{-\infty}^{\infty} f(u)\overline{\psi}\left(\frac{u-t}{s}\right)du \tag{2}$$

Where s is the scale parameter, t the position parameter, $f()$ the signal function, $\psi()$ the wavelet function and the overline represents the complex conjugate.

The complex Morlet wavelet is a complex exponential multiplied by a gaussian window, which can be used to decompose the signal into amplitude and phase components:

$$\Psi_\sigma(t) = \left(1 + \exp(-\sigma^2) - 2\exp\left(-\frac{3}{4}\sigma^2\right)\right)^{-\frac{1}{2}} \pi^{-\frac{1}{4}} \exp\left(-\frac{1}{2}t^2\right)\left(\exp(i\sigma t) - \exp\left(-\frac{1}{2}\sigma^2\right)\right) \quad (3)$$

Where the wavelet central frequency is $\sim\sigma$, and the parameter σ allows trade between time and frequency resolutions. Throughout this study I only used the complex Morlet wavelet with $\sigma = 3$, to get a higher temporal resolution at the cost of lower frequency resolution.

The scaleogram, analog to the spectrogram, is defined as the square of the amplitude of the CWT:

$$X(t,s) = W(t,s)\overline{W(t,s)} \quad (4)$$

The spectrum is defined as the integration of the amplitude of the CWT over its complete duration:

$$Y(s) = \int_{-\infty}^{\infty} \sqrt{W(t,s)\overline{W(t,s)}}dt \quad (5)$$

2.6 Conductance-based model

The CPG model developed by Jalil et al. 2010 was adapted by adding the equations 6f, 6g, 6k with their corresponding currents to the equation 6a:

$$\frac{dV_i}{dt}(t) = -\frac{I_{i,\text{Na}} + I_{i,\text{K}} + I_{i,\text{L}} + I_{i,\text{Syn}} + I_{i,\text{CCAP}}(t) + I_{i,\text{X}}}{C} \tag{6a}$$

$$I_{i,\text{Na}} = g_{\text{Na}}(V_i - E_{\text{Na}})n_i^3 h_i \tag{6b}$$

$$I_{i,\text{K}} = g_{\text{K}}(V_i - E_{\text{K}})m_i^2 \tag{6c}$$

$$I_{i,\text{L}} = g_{\text{L}}(V_i - E_{\text{L}}) \tag{6d}$$

$$I_{i,\text{Syn}} = g_{\text{Syn}}(V_i - E_{\text{Syn}})s(-1000(V_j + 0.0225)), \quad i \neq j \tag{6e}$$

$$I_{i,\text{CCAP}}(t) = g_{\text{CCAP}}(V_i - E_{\text{CCAP}})p(t) \tag{6f}$$

$$dI_{i,\text{X}} = -\frac{I_{i,\text{X}}}{\tau_{\text{X}}} + \sigma_{\text{X}} W_{i,t} \tag{6g}$$

$$n_i = s(-150(V_i + 0.0305)) \tag{6h}$$

$$\frac{dh_i}{dt} = \frac{s(500(V_i + 0.0333)) - h_i}{\tau_{\text{Na}}} \tag{6i}$$

$$\frac{dm_i}{dt} = \frac{s(-83(V_i + V_{\text{Shift}})) - m_i}{\tau_{\text{K}}} \tag{6j}$$

$$\frac{df_i}{dt} = \frac{s(-100(V_i + 0.04)) - f_i}{\tau_{\text{f}}} \tag{6k}$$

$$s(x) = \frac{1}{1 + \exp(x)} \tag{6l}$$

Where V is the membrane voltage, C the membrane capacitance and t the time. I, g, E, τ represent the current, the maximum conductance, the reversal potential and the time constant. Their subscripts i, j refer to the neuron index, Na, K, L, Syn, CCAP, X refer to Sodium, Potassium, leakage, synapse, CCAP, and noise (which is an Ornstein-Uhlenbeck process), respectively. $p(t)$ is the motoneuronal oscillation probability (equation 13). W_t represents a Wiener process and σ_{x} its volatility. n, h, m are the Sodium activating, Sodium inactivating and Potassium activating gating variables; f represents the calcium imaging fluorescent intensity. V_{Shift} is a Potassium activation curve shifting parameter.

Equation 6f was added to generate a depolarizing current during the predicted oscillatory phase. $p(t)$, the oscillating probability at time t from the logistic model approaches 0 when the oscillation probability is low and 1 when it is high. In the conductance model, $p(t)$ acts as a gating variable,

g_{CCAP} as the maximum conductance parameter and E_{CCAP} as the reverse potential. A high $p(t)$ value generates depolarizing currents that help the system reach the voltage threshold to fire action potentials (APs) in a bursting and alternating pattern between the neurons of the circuit. On the contrary, a low $p(t)$ value tends to keep the system in a non-oscillatory state.

Equation 6g adds stochasticity to the model, which has the effect of mimicking the probabilistic influence of the α CCAP neurons on the motoneuronal oscillatory activity. It also adds phase noise during the oscillatory activity, similar to the one observed in the experimental recordings (Figure 11).

Equation 6k generates fluorescence (calcium) spikes which respond with a τ_{f} time constant. The equation increases the fluorescence during the bursting phase and decreases it during the non-bursting phase.

2.7 Exponential decay time constant computation

I computed the time constant through the widespread technique of curve fitting. This was done by fitting exponential decay function templates to time series segments. The template was defined as:

$$f(t) = a \exp\left(\frac{-t}{\tau}\right) + b \tag{7}$$

Where a, b and τ are constants, a represents the amplitude of the decay, b the basal fluorescence and τ the time constant. The time constant of a segment was defined to be the τ of the fitted template, which was fitted through the least squares method:

$$d(t_0) = \int_0^{15} \left(f_{\text{MN}}(t_0 + t) - f(t)\right)^2 dt \tag{8}$$

Where $f_{\text{MN}}(t)$ is the motoneuron time series and $f(t)$ the exponential decay function (equation 7) and t_0 the time where the exponential decay segment begins.

The average time constant of the motoneuron calcium spikes exponential decay was computed using only high quality (high signal to noise ratio (SNR)) segments. The procedure to select high quality segments was adapted so that roughly only the segments I considered good enough, were selected.

The procedure is as follows:

1. Save the locations of the maximum time series value within the next 10 s of the locations where $\frac{df}{dt} > 0.02$.
2. For each location, find within the next 10 s the segment with the lowest $d(t_0)$ value and save it.
3. In case of overlapping segments, select the one with the lowest $d(t_0)$ value and discard the others.
4. Discard all segments where $d(t_0) > 0.001$.
5. Discard all segments where the fitted a constant is lower than < 0.5.

2.8 Simulation metrics

The period (P), burst duration (BD) and time delay (TD) were computed directly from the voltage time series of the model, as seen in Figure 2. The duty cycle (DC) and phase difference (PD) were calculated through the following equations:

$$DC = \frac{BD}{P} \tag{9a}$$

$$PD = \frac{360\,TD}{P} \tag{9b}$$

As the conductance model is stochastic, and the metrics vary in every cycle, they were measured for every cycle of each motoneuron. The multiple measurements generated were then used to study the distribution of the metrics.

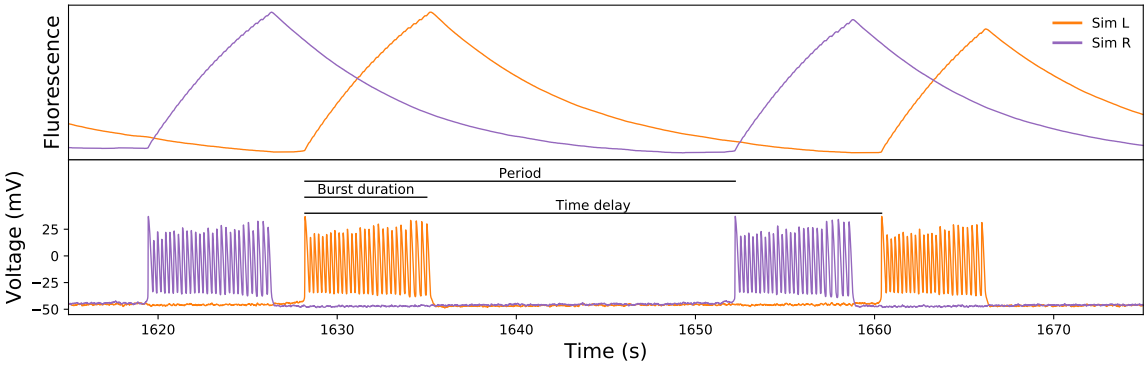

Figure 2. Simulation metrics. Top shows the Fluorescence and bottom the voltage output of the model. The period, burst duration and time delay of a single cycle of one motoneuron are shown. “Sim L” and “Sim R” indicate the left and right simulated motoneurons respectively

2.9 Statistical methods

2.9.1 p-values

I computed the p-values using the Mann-Whitney U test as implemented in the Python's SciPy library. This test is similar to the Student's t-test, but unlike the Student's t-test, it does not require that the data be normally distributed. For the same reason, I chose the Mann-Whitney U test over the more widespread Student's t-test as in many cases the distribution did not appear to be normal. The drawback of Mann-Whitney U test is that some statistical power is lost when contrasted to the Student's t-test on a normal distribution.

2.9.2 Correlations

I measured associations between variables using Pearson's correlation as implemented in the Python's NumPy library. This correlation method is the simplest approach to measure the linear relationship between variables. This approach allowed me to detect significant results in many situations, and in contrast to non-linear methods, its results are easier to interpret, because of the linear nature of the computation.

2.9.3 Classification error rate

I used classification error rate (CER) as a first approximation to evaluate the quality of a model. The CER indicates the proportion of misclassifications, and is defined as:

$$CER = \frac{FP + FN}{P + N} \tag{10}$$

Where FP, FN, P and N represent the false positives, false negatives, positives and negatives respectively. The best models tend to have lower CER values, but this metric only sees a small part of the model, as it needs to be binarized at a defined threshold prior to the computation of the metric.

2.9.4 Receiver operating characteristic analysis

To solve the limitation of the CER, I computed the area under the curve (AUC) of the receiver operating characteristic (ROC) curve:

$$AUC = \int_{-\infty}^{\infty} TPR(T)FPR'(T)\,dT \tag{11}$$

Where $TPR'(T)$ is the threshold dependent true positive rate function, $FPR(T)$ is the threshold dependent false positive rate function, and T is the threshold. ROC curves have the advantage of showing the relation between the true positive rate (TPR) (proportion of positives that are correctly identified as such) and false positive rate (FPR) (proportion of negatives that are wrongly identified as such) at different thresholds after binarization. The best models tend to have the higher AUC values.

2.9.5 Akaike information criterion

To select models, I used the akaike information criterion (AIC) (Akaike 1974), an estimator used to select the best model by taking into account the tradeoff between the goodness of the fit and the complexity of the model. The AIC value of a model is:

$$AIC = 2k - 2\log(L) \tag{12}$$

Where k is the number of parameters of the model and L is the maximum likelihood of the model. Given a set of models, the preferred model is the one with the minimum AIC value.

3 Results

3.1 Neuronal dynamics

3.1.1 Calcium time series

Calcium fluorescence images from CCAP neurons only, and from CCAP neurons together with motoneurons (Figure 3a, b) after the preparations were stimulated with ETH were provided by Wilson Mena. I developed and applied a stabilization algorithm to the video recordings to reduce measurement noise introduced by tissue drifting and deformation (Methods, section 2.2).

(a) **(b)**

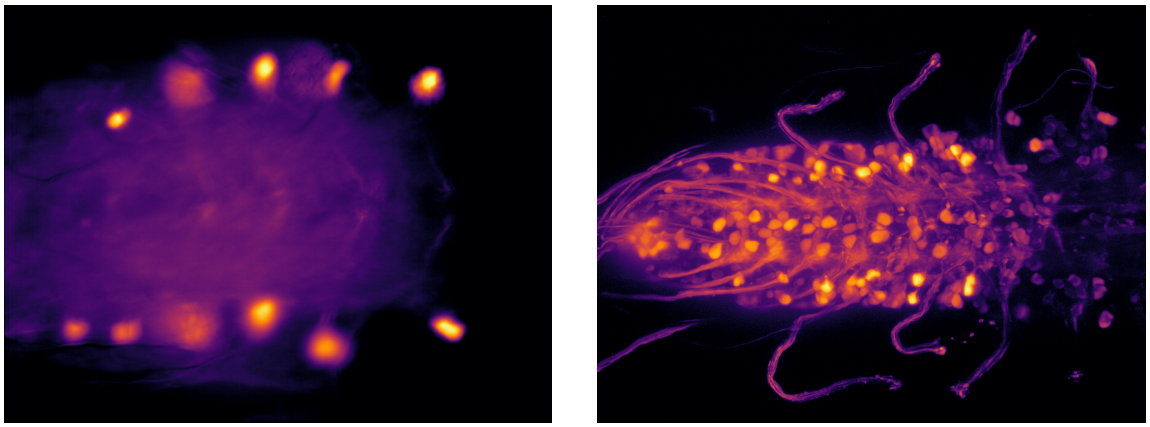

Figure 3. Calcium imaging. (a) Single slice calcium imaging of CCAP neurons. **(b)** Merged 5-slices calcium imaging stack of CCAP neurons and motoneurons.

I generated the time series with ImageJ (Rasband 2013) by computing the intensity mean of the regions of interest (ROIs). CCAP neuron ROIs contained single neurons while motoneuron ROIs contained groups of neurons of either the left or the right region. I grouped motoneurons of each side because they showed similar activity and grouping them increased the SNR and made the task of finding the same neurons in different experiments easier. I preprocessed the raw calcium time series generated by ImageJ through detrending and normalization to reduce the experimental noise (Methods, section 2.3), and as a last step I resampled the time series linearly to 1 s intervals (Figure 4).

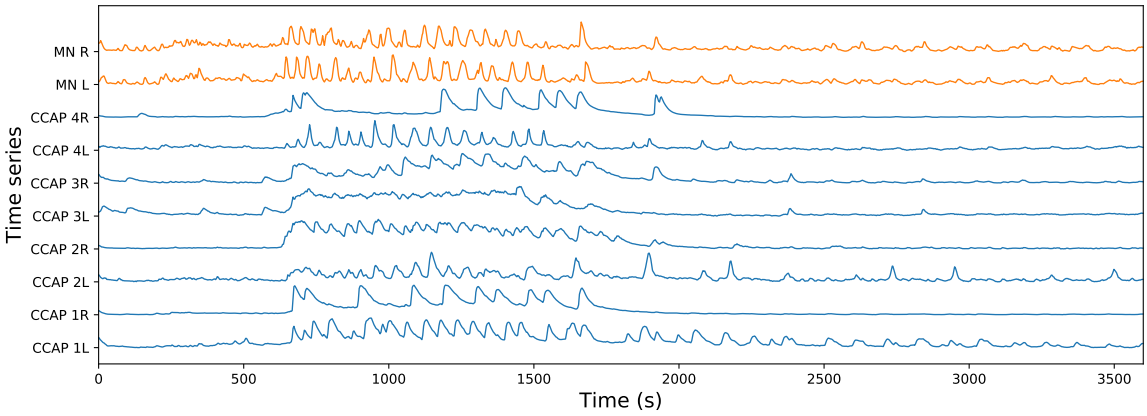

Figure 4. Calcium imaging time series. Sample of time series of the calcium sensitive fluorescence of AN1-AN4 α CCAP neurons and motoneurons one hour post-ETH-stimulation. "MN" and "CCAP" indicate motoneurons and α CCAP neurons respectively. The letter indicates the side (left/right), while the number indicates the abdominal segment of the neurons.

3.1.2 Individual dynamics

Before performing advanced analyses, I began with the simplest ones, with minimal assumptions on the form of the data. I started characterizing the signal patterns individually, which also is part of my first objective.

The onset of the motoneuronal alternating activity has been associated with the beginning of the ecdysis phase (Kim et al. 2006; Mena et al. 2016). To see if the hypothesis, that α CCAP neurons and motoneurons have coordinated activity holds, I computed their onset. Unlike previous works (Kim et al. 2006; Mena et al. 2016), here I computed the onset of the two populations of neurons within the same experiment.

This was done by determining the instant when a filtered fluorescence time series reached the threshold of 1/2 of the maximum unfiltered time series fluorescence (Methods, section 2.4, Figure 5a).

I found that the mean onset of α CCAP neurons and motoneurons from the same experiment tended to be temporally close to each other, suggesting that α CCAP neurons initiate the motoneuronal activity (Figure 5b, Table 2, 3, 4). Motoneurons tended to initiate their activity after a few α CCAP neurons had already initiated their activity, suggesting that some level of α CCAP activity is required to initiate the motoneuronal oscillatory activity. I computed the p-values with the non-parametric Mann-Whitney U test, analog to the Student's t-test, but without the normal distribution requirement. I used the one-tailed Mann-Whitney U test to compare the onset difference between α CCAP neurons and motoneurons of

each experiment to the null cross-experiment difference between the two neuron populations. I found that for all experiments except one, the onset of α CCAP neurons and motoneurons was significantly temporally close. The mean onset (n = 9) was 1176 s for the α CCAP neurons and 1150 s for the motoneurons.

These results are in agreement with non-simultaneous experimental recordings and measurements of the activity onset of α CCAP neurons and motoneurons (Mena et al. 2016), but more strongly suggest that the two populations of neurons have coordinated activity.

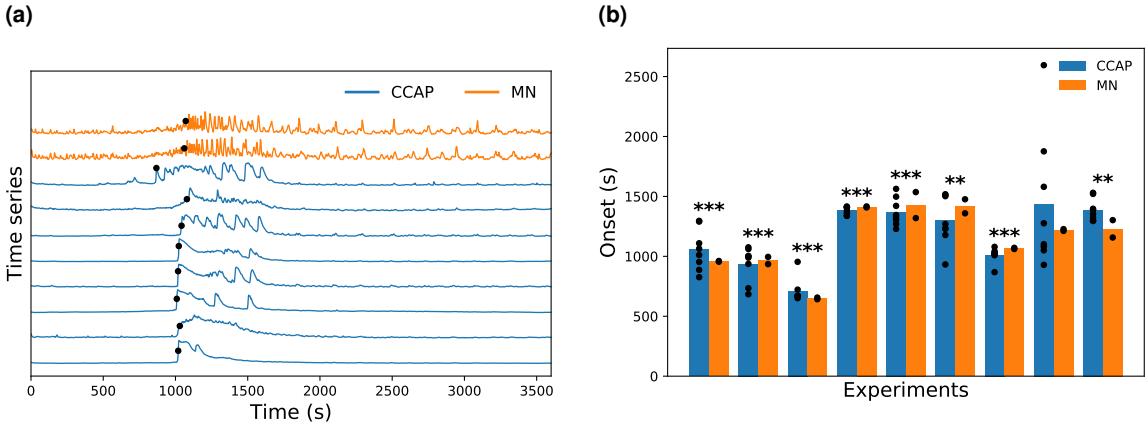

Figure 5. Activity onset. (a) Sample of activity onset of α CCAP neurons and motoneurons of a single experiment. **(b)** Mean onset of α CCAP neurons and motoneurons showing temporally close values between populations in each of the 9 experiments. "MN" and "CCAP" indicate motoneurons and α CCAP neurons respectively. **: p-value < 0.01, ***: p-value < 0.001.

	Experiment								
Neuron	1	2	3	4	5	6	7	8	9
1L	826	734	670	1379	1270	1270	1019	2595	1298
1R	887	1075	670	1407	1421	1229	1030	929	1295
2L	1064	1003	954	1338	1498	932	1009	1050	1521
2R	953	684	651	1338	1328	1233	1018	1082	1322
3L	1109	1001	668	1416	1305	1178	1023	1276	1387
3R	1011	937	671	1360	1345	1511	1042	1101	1353
4L	1290	1061	722	1410	1229	1502	1079	1580	1530
4R	1296	989	669	1409	1563	1518	868	1876	1397
Mean	1054	936	709	1382	1370	1297	1011	1436	1388
SEM	61	52	36	12	41	72	22	199	33

Table 2. α CCAP neuron activity onset. Onset (s) values of Figure 5b. The letter indicates the side (left/right), while the number indicates the abdominal segment of the neuron.

	Experiment								
Neuron	1	2	3	4	5	6	7	8	9
L	961	995	642	1416	1319	1359	1061	1227	1302
R	955	935	656	1408	1536	1476	1071	1212	1157
Mean	958	965	649	1412	1428	1418	1066	1220	1230
SEM	3	30	7	4	108	58	5	8	72

Table 3. Motoneuron activity onset. Onset (s) values used in Figure 5b. The letter indicates the side (left/right) of the motoneurons.

	Experiment								
	1	2	3	4	5	6	7	8	9
p-value	<0.001	<0.001	<0.001	<0.001	<0.001	0.008	<0.001	0.404	0.001

Table 4. Onset coordination p-values. p-values of Figure 5b.

To better characterize the neuronal activity, and taking advantage of the oscillatory activity of both neuron populations, the periods of their oscillations were computed.

To convert the data from the time domain to the time-frequency domain I used the CWT (Methods, section 2.5) instead of the more widespread Fourier transform, as the latter cannot localize the frequency components in time. And even though I did not always require the time dimension component, I decided to use a single method in all analyses of this study for consistency.

To get a first approximation of the period of the α CCAP neurons, and taking into account their highly irregular activity pattern, I computed the average scaleogram (Methods, section 2.5) of all recorded α CCAP neurons (n = 111) (Figure 6a). I found that the main oscillatory period was around 50 s to 200 s.

To get a more detailed characterization of their period I decided to study the individual α CCAP periods by computing their spectra (Methods, section 2.5). I then discarded the spectra where there was no clear highest single frequency component. If the amplitude in the intervals between half the maximum amplitude period and the maximum amplitude period, or between the maximum amplitude period and twice the maximum amplitude period did not drop lower than 80 % of the maximum value, the spectrum was discarded (Figure 6b). Only the 47 % of the neurons passed the selection criteria, which evidenced the irregularity of the oscillatory activity of these neurons (Figure 6c, Table 5). Neurons that passed the selection criteria tended to display a clear predominant oscillatory component, as opposed to the discarded records, which tended to show more irregular activity, lower SNR, or a mixture of several oscillatory components. The mean oscillatory period for all these neurons was 166 s (n = 13, SEM = 23.3 s) which was consistent with previous rough estimation from Figure 6a.

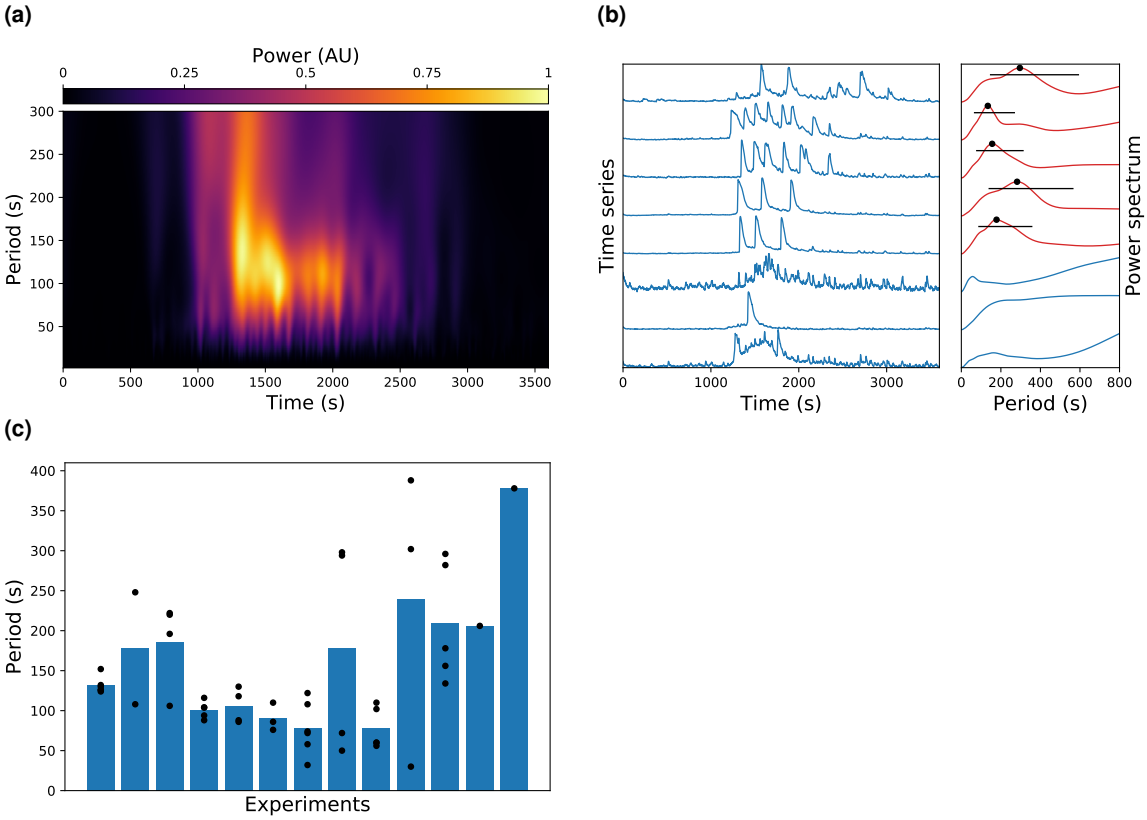

Figure 6. Oscillation periods of α CCAP neurons. **(a)** Average scaleogram for all α CCAP neuron time series. **(b)** Left shows time series of 8 α CCAP neurons of a single experiment. Right shows their corresponding spectrum computed with the CWT. The dot shows the maximum spectrum value; the threshold line shows the 80 % of the maximum value and span between half and twice the period of the maximum spectrum value. Accepted α CCAP neuron recordings intersect the threshold line at both sides of the dot and are colored in red. **(c)** Mean oscillation period of the accepted neurons of 13 experiments.

Neuron	Experiments												
1L	126	108	220	104	—	110	74	—	60	388	—	—	—
1R	152	—	106	88	—	76	72	—	—	—	—	—	—
2L	124	—	222	94	—	—	108	50	60	—	—	—	—
2R	132	—	—	104	—	86	122	—	—	—	178	206	—
3L	130	—	196	116	88	—	—	72	—	30	282	—	—
3R	126	—	—	—	86	—	58	—	102	302	156	—	—
4L	—	—	—	—	130	—	—	298	56	—	134	—	378
4R	—	248	—	—	118	—	32	294	110	—	296	—	—
Mean	132	178	186	101	106	91	78	178	78	240	209	206	378
SEM	4	70	27	5	11	10	13	68	12	108	33	—	—

Table 5. α CCAP neuron periods. Period (s) values of Figure 6c. Same notation as in Table 2 was used.

I computed the average scaleogram for all motoneuron time series (n = 18) and found that they oscillate at lower periods than α CCAP neurons (Figure 7a). Their mean period was around 25 s to 50 s.

I then measured the left and right motoneuron regions the same way as I did for the α CCAP neurons and obtained an average value of 33.4 s (n = 11, SEM = 4.1 s) (Figure 7b, Table 6). In contrast to α CCAP neurons, motoneurons displayed a more regular pattern of activity with a clearer main oscillatory component, and no motoneurons were discarded by the selection criteria. The difference between the left and right region principal oscillatory period was also smaller that for α CCAP neurons of a single experiment, which could be attributed to the apparent similar but phase shifted oscillatory activity, also suggesting that their activity is not independent.

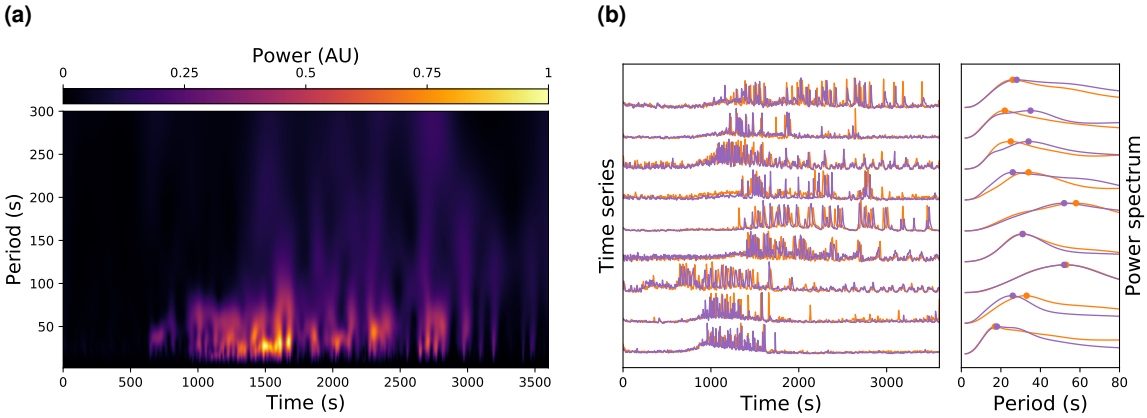

Figure 7. Oscillation periods of motoneurons. **(a)** Analog to Figure 6a, but with motoneurons. **(b)** Analog to Figure 6b, the main oscillatory component of motoneurons of 9 experiments were computed, and show minimal differences between the left and right region motoneurons.

	Experiment								
Neuron	1	2	3	4	5	6	7	8	9
L	17.0	33.0	53.0	31.0	58.0	34.0	25.0	22.0	26.0
R	18.0	26.0	52.0	31.0	52.0	26.0	34.0	35.0	28.0
Mean	17.5	29.5	52.5	31.0	55.0	30.0	29.5	28.5	27.0
SEM	0.5	3.5	0.5	0.0	3.0	4.0	4.5	6.5	1.0

Table 6. Motoneuron periods. Period (s) values of Figure 7b. Same notation as in Table 3 was used.

These results show that even when α CCAP neurons and motoneurons tend to initiate their activity at the same instant, they oscillate with different periods. One possible explanation could be that α CCAP neurons activate a CPG that generates motoneuronal oscillations at a different frequency; this

would also explain why the left and right region motoneurons from a single recording oscillate with a similar period. α CCAP neurons also display similar oscillatory periods suggesting that their activity is coordinated, which could be caused by an autocrine feedback loop. The autocrine action is in agreement with the work of Mena et al. 2016, where he shows that PBURS affects the activity pattern of the CCAP neurons.

3.1.3 CCAP neuronal coordination

As shown in the previous section, α CCAP neurons show coordinated activity; I measured the linear relationship of their time series using Pearson's correlation, which is also the simplest approach to measure association between variables. This approach also worked very well as it allowed me to detect many statistical significant results.

I began computing the correlation between each pair of neurons within each of the 9 experiments and found a high variability in the correlation matrices of the different experiments (Figure 8). I hypothesized that the high variability could be the result of multiple factors such as: variability in the neuronal activity patterns, ambiguous identification of neurons, neighbouring neural fluorescence interference, tissue drifting and deformation, damage caused by the extraction or manipulation of the CNS and low SNR.

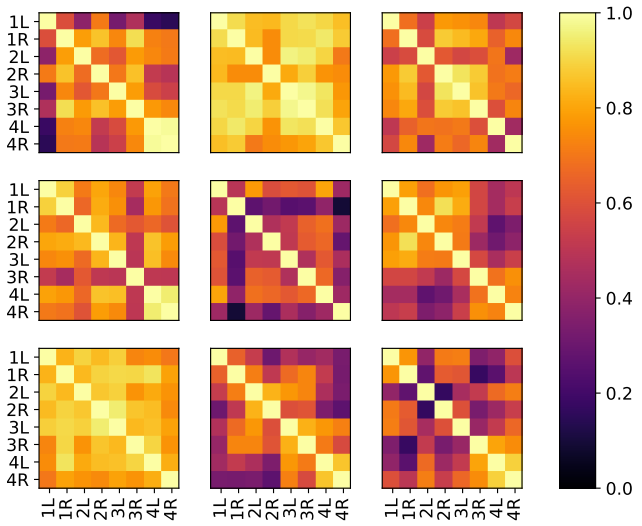

Figure 8. CCAP neuron correlation matrices. Pearson's correlation coefficient matrices of α CCAP neuron time series of 9 experiments. Same notation as in Table 2 was used.

To increase the statistical power of my analyses, I grouped the correlation pairs into functionally equivalent pair groups, based on what it is known about their anatomy, and synaptic and peptidergic connectivity.

CCAP neurons can be classified into 5 morphologically distinct groups, but AN1-AN4 α and β CCAP neurons form part of 2 of these groups (Karsai et al. 2013). The somas of α and β neurons tend to be close to each other, but α and β neurons tend to occupy a more ventrolateral and a more dorsolateral position respectively (Karsai et al. 2013; Santos et al. 2007). α and β neurons project medially and display a dense arborization between the ventromedial and dorsomedial region (Karsai et al. 2013; Santos et al. 2007). α neurons send projections from the medial region to peripheral neurohemal release sites (Karsai et al. 2013). β neurons project from the medial region to the contralateral region, where they branch in a T-shape, to project anterior and posterior along the ventrolateral tract (ibid.).

Much less is known about how these neurons communicate, but immunostaining techniques have shed some light on their communication mechanisms (Karsai et al. 2013; Loveall and Deitcher 2010; Santos et al. 2007). α neurons present synaptic inputs at the medial arborization and likely synaptic outputs as well (Karsai et al. 2013). Their peripheral neurohemal type III terminals on the body wall muscles release Bursicon, CCAP and MIPs (Loveall and Deitcher 2010). The β neuron medial arborization contains input and output sites and it is suggested that α and β neurons form synaptic connections in this region (Karsai et al. 2013). β neurons contain input and output sites plus CCAP release sites (ibid.) at the ventrolateral fibre and also form reciprocal synapses between them (ibid.).

Based on this anatomical information, I grouped the correlation pairs into 3 groups: contralateral neurons, ipsilateral neurons and "other" neuron pairs (containing the pairs that do not fall into the other 2 categories) (Figure 9a). I grouped contralateral neurons together because they converge in the medial arborization of each segment. I grouped ipsilateral neurons because β neurons form reciprocal synapses at their contralateral side, which could also coordinate ipsilateral α neurons through the medial arborization.

I computed the mean correlation of each group in the time domain and in the time-frequency domain (through the CWT) (Figure 9b, c, d, e, f, Table 7). The correlations in the time-frequency domain were performed in two different ways, by looking into the amplitude component (the absolute value of the complex number), and into the amplitude and phase components of the signal (the real part of the complex number). I computed the group p-values using the one-tailed Mann-Whitney U test to compare correlations of each experiment to null cross-experiment correlations. In all cases the p-values were

< 0.001 as it can be seen in the table, making group correlations in Figure 9b, c, d, e, f highly significant. The p-values between the three groups were computed using the two-tailed Mann-Whitney U test.

I found that the Pearson's correlation coefficients mean of the three groups of α CCAP neurons in the time domain were high ($r > 0.61$) (Figure 9b). I also found a significant higher level of association between contralateral neurons compared to ipsilateral neurons (p-value < 0.04) and compared the "other" pair group (p-value < 0.02). These results suggest that the tightest coupling appears to be through the medial arborization.

I performed the same test with β neurons and found the coefficients mean to be even higher ($r > 0.73$) with lower dispersion than for α neuron pairs (Figure 9c). The contralateral pairs showed a significantly higher correlation than the "other" pairs (p-value < 0.005). These results suggest that the contralateral coupling through the medial arborization is not significantly different than the ipsilateral coupling through the contralateral reciprocal synapses.

To test the level of association between α and β neurons, the pairing for each group was made between an α and β neuron. The coefficients mean ($r > 0.62$) showed that the contralateral group had a significantly higher correlation than the ipsilateral and the "other" group (p-values < 0.007 and < 0.005 respectively) (Figure 9d). Just like in $\alpha\alpha$ pairs, the tightest coupling appears to be through the medial arborization.

To reduce the effect of noise in the correlation of the α neuron time series, I studied their association in the time-frequency domain in the 50 s to 200 s period band. This also allowed me to study the correlation of the amplitude with and without the phase component. The conversion to the time-frequency domain was performed at 100 linearly distributed periods.

The coefficient means of the amplitude (absolute value of the CWT) of the oscillations were lower than in the time domain ($0.44 < r < 0.59$) (Figure 9e). One possible explanation for the correlation drop could be that the higher correlation in the time domain was partially caused by low frequency component synchronization caused by the increase of calcium fluorescence during the ecdysis phase. In contrast to the time domain, the significance of the correlation differences increased. I found that the contralateral group had significantly higher correlation than the ipsilateral and the "other" group (p-values < 0.001).

To measure the effect of the phase in the coordination of the α neurons I repeated the same procedure, but this time I looked at the amplitude and phase (the real component of the CWT) of the oscillations at the same time. I found that the correlation coefficient means dropped even further

(0.15 < r < 0.28), suggesting that the phase of the oscillations was poorly coordinated (Figure 9f). Contralateral and "other" group kept the significantly higher correlation (p-value < 0.04).

These results show that all AN1-AN4 CCAP neurons tend to have synchronized activity, but their coupling strength varies depending on the neuronal pair. αα and αβ pairs appear to show higher coupling through the medial arborization, while ββ pairs show similar contralateral and ipsilateral coupling strength.

To test if the distance between the neurons affects the strength of the coupling, I divided the pairs into 3 ipsilateral groups based on their segment separation. The I1, I2 and I3 groups contain ipsilateral pairs of contiguous, separated by 1 and separated by 2 segments respectively. I performed the same analyses on these groups (Figure 9g, h, i, j, Table 8).

αα neuron pairs show in the time-frequency domain a coupling strength that drops as the segmental distance increases (Figure 9j). ββ neuron pairs on the other side do not appear to be affected by the increase in distance, which could suggest that neurons of different segments form reciprocal connections in the contralateral region in an homogenous way (Figure 9h). αβ pairs also show a decrease of their coupling as their distance increases (Figure 9i). The reason why the strength of the coupling of the pairs with α neurons drops as distance increases is harder to hypothesize as their connectivity is not direct; the reason behind this may involve other neurons or peptidergic diffusion.

As it can be seen, the connectivity between different AN1-AN4 CCAP neurons is highly complex in anatomical (Karsai et al. 2013; Loveall and Deitcher 2010; Santos et al. 2007) and functional terms (as shown here). This, added to the incomplete picture of the circuit, makes it especially difficult to propose a connectivity model that explains the observed coupling between these neurons. My findings in the coupling of these neurons can be summed up into the following points:

- Contralateral neurons tend to be highly coupled, probably through the medial arborization.
- Ipsilateral β neurons are highly coupled, probably through the contralateral reciprocal synapses.
- α neurons are oscillation amplitude coupled but not oscillation phase coupled, suggesting that they generate the oscillatory activity independently.
- Segmental distance reduces the coupling in all pairs except the ββ pairs, probably because these neurons are reciprocally synaptically connected in the contralateral region.

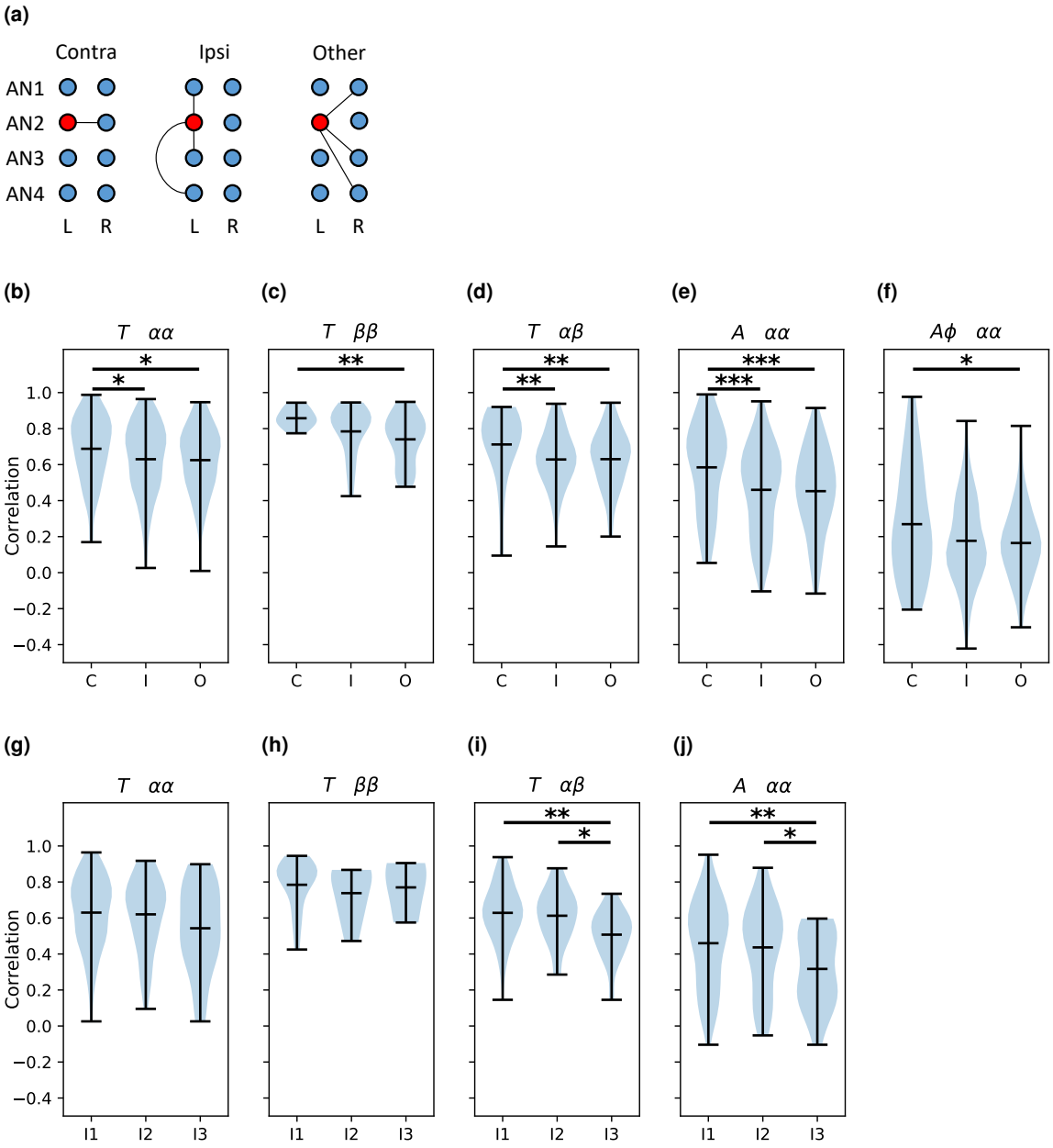

Figure 9. CCAP neuron coordination. **(a)** Pearson's correlations pairs are divided into 3 groups: Contralateral neurons ("C"), ipsilateral neurons ("I"), and "others" ("O"). As an example, the graph shows to what group a pair, that has a left AN2 neuron, would belong to. **(b-f)** Correlation coefficients between time series of CCAP neurons are shown as violin plots with their minimum, maximum and mean values. **(b)** shows α CCAP neurons in the time domain. **(c)** β shows CCAP neurons in the time domain. **(d)** α and β CCAP neurons pairs in the time domain. **(e)** α CCAP neurons amplitude of oscillations in the time-frequency domain. **(f)** α CCAP neurons amplitude and phase in the time-frequency domain. **(g-j)** Correlation between ipsilateral pairs at different segmental separation, "I1", "I2" and "I3" groups are contiguous, separated by 1 and separated by 2 segments respectively. The plots use the same notation as the **(b-f)** plots. *: p-value < 0.05, **: p-value < 0.01, ***: p-value < 0.001.

						inter-group p-value		
Domain	Pair	Group	Corr.	n	p-value	C	I	O
T	αα	C	0.69	52	<0.001	—	0.036	0.012
T	αα	I	0.63	150	<0.001	0.036	—	0.336
T	αα	O	0.62	148	<0.001	0.012	0.336	—
T	ββ	C	0.86	12	<0.001	—	0.115	0.004
T	ββ	I	0.78	27	<0.001	0.115	—	0.054
T	ββ	O	0.74	29	<0.001	0.004	0.054	—
T	αβ	C	0.71	18	<0.001	—	0.006	0.004
T	αβ	I	0.63	73	<0.001	0.006	—	0.428
T	αβ	O	0.63	76	<0.001	0.004	0.428	—
A	αα	C	0.58	52	<0.001	—	<0.001	<0.001
A	αα	I	0.46	150	<0.001	<0.001	—	0.354
A	αα	O	0.45	148	<0.001	<0.001	0.354	—
Aϕ	αα	C	0.27	52	<0.001	—	0.051	0.039
Aϕ	αα	I	0.18	150	<0.001	0.051	—	0.406
Aϕ	αα	O	0.16	148	<0.001	0.039	0.406	—

Table 7. CCAP correlation coefficients (contralateral, ipsilateral, "other"). Values of Figure 9b, c, d, e, f. Same notation as in Figure 9 was used.

						inter-group p-value		
Domain	Pair	Group	Corr.	n	p-value	I1	I2	I3
T	αα	I1	0.63	150	<0.001	—	0.403	0.057
T	αα	I2	0.62	49	<0.001	0.403	—	0.126
T	αα	I3	0.54	23	<0.001	0.057	0.126	—
T	ββ	I1	0.78	27	<0.001	—	0.210	0.459
T	ββ	I2	0.74	8	0.018	0.210	—	0.459
T	ββ	I3	0.77	3	0.024	0.459	0.459	—
T	αβ	I1	0.63	73	<0.001	—	0.344	0.003
T	αβ	I2	0.61	26	<0.001	0.344	—	0.015
T	αβ	I3	0.51	15	0.007	0.003	0.015	—
A	αα	I1	0.46	150	<0.001	—	0.271	0.004
A	αα	I2	0.44	49	<0.001	0.271	—	0.027
A	αα	I3	0.32	23	0.031	0.004	0.027	—

Table 8. CCAP correlation coefficients (Ipsilateral distance). Values of Figure 9g, h, i, j. Same notation as in Figure 9 was used.

3.1.4 Motoneuronal coordination

As the left and right motoneuronal regions appeared to have synchronous but phase shifted activity, I calculated the Pearson's correlation coefficients of pairs of motoneuronal region time series (n = 9). I found, against my expectations, that the coefficients were positive for all experiments (Table 9). I hypothesized that the positive coefficients were the result of the synchronous increase of fluorescence during the ecdysis phase, and common noise (noise affecting both regions in the same way).

	Experiment										
	1	2	3	4	5	6	7	8	9	Mean	SEM
Correlation	0.67	0.42	0.27	0.12	0.35	0.25	0.49	0.36	0.14	0.34	0.06

Table 9. Motoneuronal correlation. Correlation between left and right motoneuronal regions of 9 experiments.

To test my hypothesis and also better visualize the way motoneurons synchronize during the different phases, I computed the Pearson's correlation between the regions on a sliding window of 100 s (Figure 10). The window size value was chosen so that it was greater than the oscillation period, but lower than the oscillation bursts duration. I found that the correlations tended to be negative during the oscillating periods and positive during the non-oscillating periods, thus confirming my hypothesis.

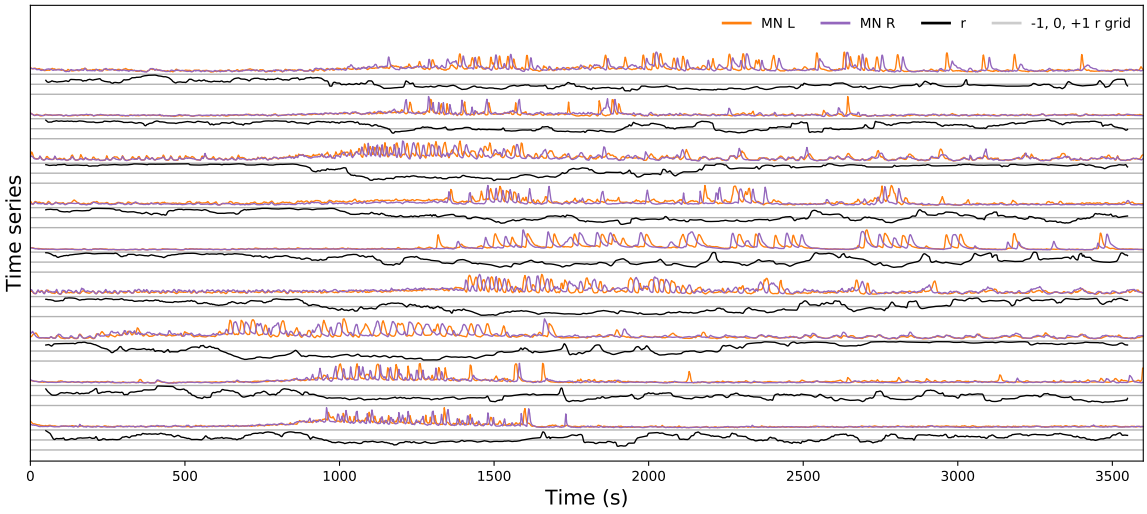

Figure 10. Motoneuronal sliding window correlation. Correlation coefficient time series of sliding windows of 100 s. Time series of left ("MN L") and right ("MN R") motoneuronal regions are shown in orange and purple and the Pearson's correlation coefficient ("r") of the sliding window is shown in black. Gray horizontal lines indicate correlations of –1, 0 and 1.

To better characterize the motoneuronal left-right region synchrony, I studied their phase difference, which I hypothesized should be close to 180°. I used the CWT to compute the instantaneous amplitude and phase in their primary oscillatory period (mean values of Table 6). I then generated vectors with angles equal to the phase difference and lengths equal to the mean amplitude of their CWT. The phase difference of the regions was computed by averaging all the vectors of the experiment (Figure 11a).

I found a great level of phase difference variability within each experiment, and also an important spread of the experimental mean phase difference (Figure 11b, Table 10), with a global mean of 182.1° (SEM = 14.6°).

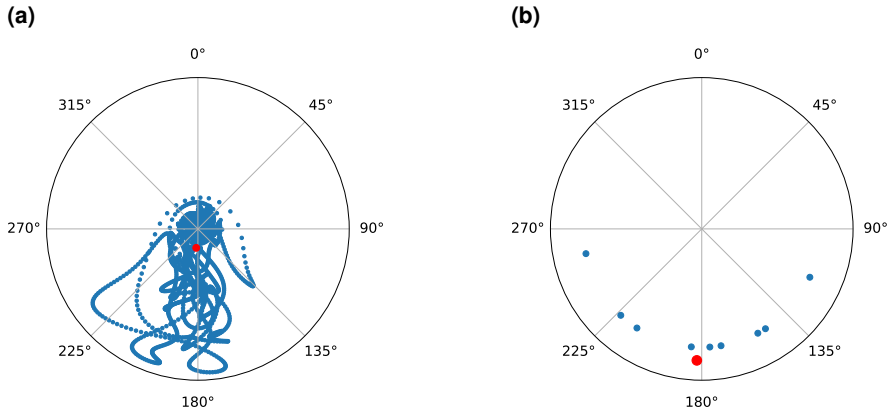

Figure 11. Motoneuronal phase difference. (a) Example of the method used to compute the mean phase difference of an experimental recording. Blue points represent the phase difference at every instant of the experiment, their amplitude is scaled to the mean amplitude of the oscillations of the left and right region signals. The red point represents the mean vector, whose phase represents the mean phase difference of the experiment. **(b)** Mean phase difference for 9 experiments in blue and the mean of all experiments in red.

	Experiment										
	1	2	3	4	5	6	7	8	9	Mean	SEM
Phase difference (°)	170.6	223.1	151.7	185.1	147.5	176.1	114.1	257.9	213.2	182.1	14.6

Table 10. Motoneuronal phase difference. Values of Figure 11b.

These results confirm that the motoneurons oscillate in antiphase, which is in agreement with the hypothesized existence of a CPG downstream the CCAP neurons. The irregularity of the phase difference could be an indicator that the CPG has difficulties synchronizing motoneurons without sensory feedback.

In the remainder of the thesis I used a single motoneuronal signal, made by the subtraction of the time series of one region from the other (Figure 12). The reason for this decision, is that the subtraction reduces the common noise, increases the SNR and the oscillation amplitude, without much loss of information as the two time series are mostly redundant.

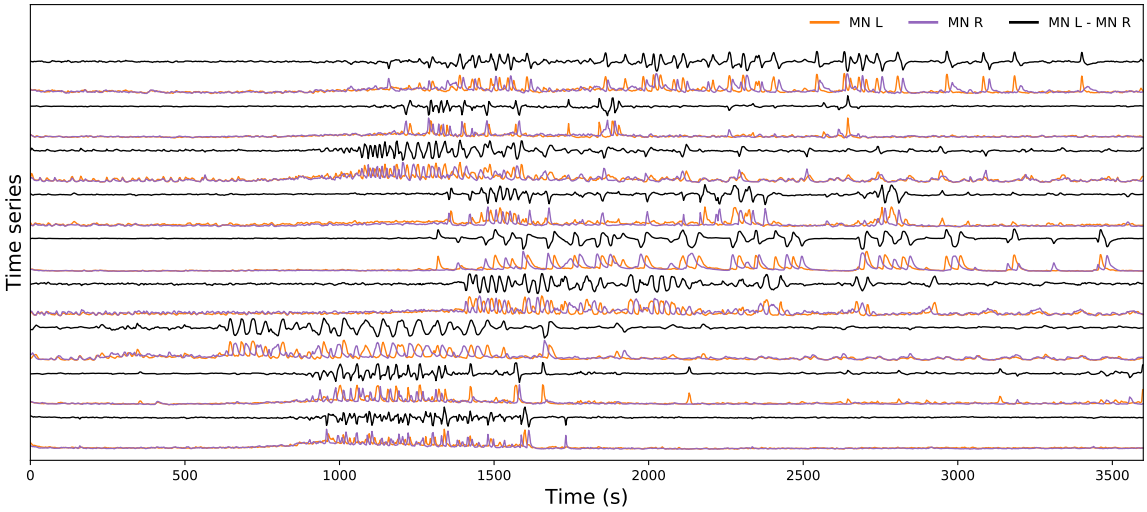

Figure 12. Motoneuronal subtraction signal. Motoneuronal signal ("MN L - MN R") generated by the subtraction of the right motoneuronal region signal ("MN R") from the left motoneuronal region signal ("MN L").

3.1.5 Functional connectivity between CCAP neurons and motoneurons

In previous analyses of the first objective, I found that CCAP neurons and motoneurons initiate their activity roughly at the same time, but oscillate at different frequencies, I also found that the left and right motoneurons show coordinated antiphase activity. These findings suggest that CCAP neurons regulate a CPG that generates the oscillatory activity of the left and right motoneurons. As a second objective I characterized the functional connectivity between α CCAP neurons and motoneurons.

Since the two populations of neurons oscillate at different frequencies, computing the correlations of their fluorescence would not give meaningful results. While visually inspecting the time series, I noticed that α CCAP neurons appeared to modulate the amplitude of the motoneuronal activity; high levels of α CCAP neuron fluorescence tended to temporally match motoneuronal oscillations. Based on this observation I converted the motoneuronal signal so that it could be correlated to the CCAP neuron activity in a meaningful way.

To do so, I converted the motoneuronal signals into oscillation amplitude signals. This was done computing the absolute value of the CWT of the motoneuronal signal at its primary oscillatory period (mean values of Table 6) (Figure 13a). The motoneuronal oscillation amplitude signal of each experiment was then correlated using Pearson's correlation to the α CCAP neuron time series (Figure 13b, Table 11).

To compute the significance of the correlations, I computed the p-values using a one-tailed Mann-Whitney U test to compare correlations of each experiment to null cross-experiment correlations. For all experiments except one, the correlations were significant. I examined the experiment that did not display a significant correlations, and found that it was probably caused by post-ecdysis motoneuronal oscillations that did not temporally match an increase of the α CCAP activity (as seen in Figure 4).

As the onset of activity varied across experiments, it could be argued that the high significance of the correlation between α CCAP neurons and motoneurons is caused by the matching onset times. To test this hypothesis, I first computed the motoneuron oscillatory state time series and then removed the initial non-oscillatory block for each experiment.

The motoneurons were defined to be in an oscillatory state on every instant where their maximum oscillation amplitude in the 2 s to 80 s period band surpassed an arbitrarily defined threshold. The amplitudes of the oscillations were computed by calculating the absolute values of the CWT. A single threshold was used for all experiments and adjusted so that it subjectively better detected the oscillatory activity of the motoneurons (Figure 13c).

The resulting time series ended up with a duration of $\sim$2200 s (Figure 13d). I then repeated the computation of the correlation coefficients and the p-values, but on the modified time series (Figure 13e, Table 12). For all experiments except two, the results were significant suggesting that α CCAP neurons regulate the motoneuronal activity during the complete recording.

I looked into the experiment that had a significant correlation before the removal of the non-oscillatory block, and found that it lost its significance after because the significance was mostly the result of the temporal match at the initiation of the ecdysis phase. In this experiment, the matching between the motoneuronal activity and α CCAP neurons was poor during the post-ecdysis phase (Figure 14). As consequence, the low correlation coefficients between both population of neurons of the experiment did not allow the Mann-Whitney U test to discard the null hypothesis.

These results show that α CCAP neurons are functionally coupled to motoneurons, and suggest that the ecdysis CPG does not operate in a ballistic manner, and requires constant input from the α CCAP neurons to keep its ongoing oscillatory activity.

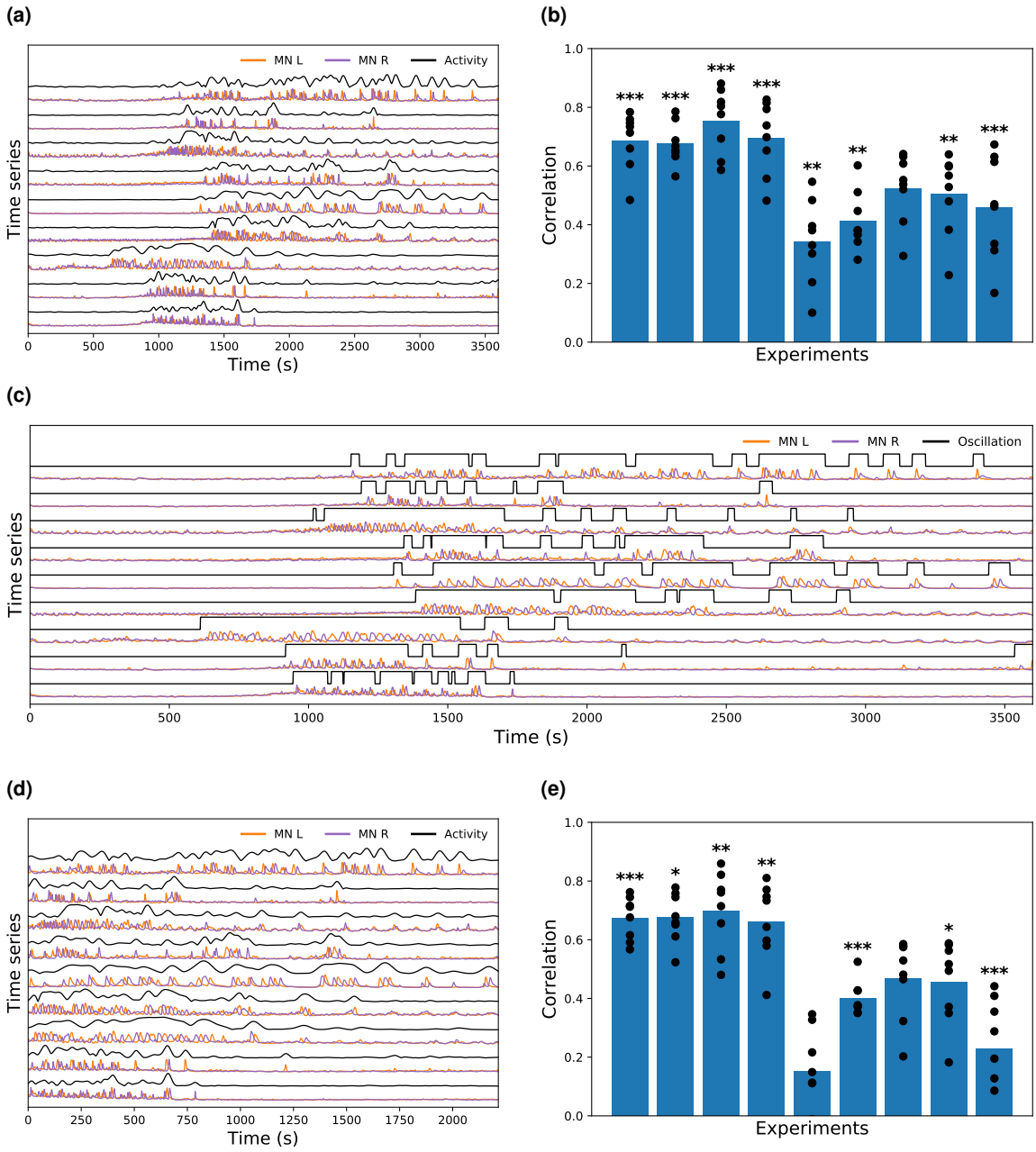

Figure 13. Correlation between α CCAP neurons and motoneurons. **(a)** Orange and purple lines show the activity of the left ("MN L") and right ("MN R") motoneuronal regions, respectively, the black line ("Activity") shows the amplitude of the motoneuronal signal. **(b)** Correlation coefficients between α CCAP neurons and the amplitude of the motoneuronal signal shown as points, and the means as bars. **(c)** Output of motoneuronal the oscillation detection algorithm. Activity from left ("MN L") and right ("MN R") motoneuronal regions are shown in orange and purple, the oscillatory state ("Oscillation") is shown in black. **(d)** Similar to **(a)**, but with pre-ecdysis phase removed. **(e)** Analog to **(b)**, but using the the time series of **(d)**. *: p-value < 0.05, **: p-value < 0.01, ***: p-value < 0.001.

	Experiment										
	1	2	3	4	5	6	7	8	9	Mean	SEM
Corr.	0.69	0.68	0.75	0.70	0.34	0.41	0.52	0.50	0.46	0.56	0.05
p-value	$<$0.001	$<$0.001	$<$0.001	$<$0.001	0.009	0.005	0.240	0.001	$<$0.001		

Table 11. Correlation between α CCAP neurons and motoneurons (with pre-ecdysis). Values of Figure 13b.

	Experiment										
	1	2	3	4	5	6	7	8	9	Mean	SEM
Corr.	0.67	0.68	0.70	0.66	0.15	0.40	0.47	0.46	0.23	0.49	0.07
p-value	$<$0.001	0.018	0.007	0.006	0.447	$<$0.001	0.602	0.031	$<$0.001		

Table 12. Correlation between α CCAP neurons and motoneurons (without pre-ecdysis). Values of Figure 13e.

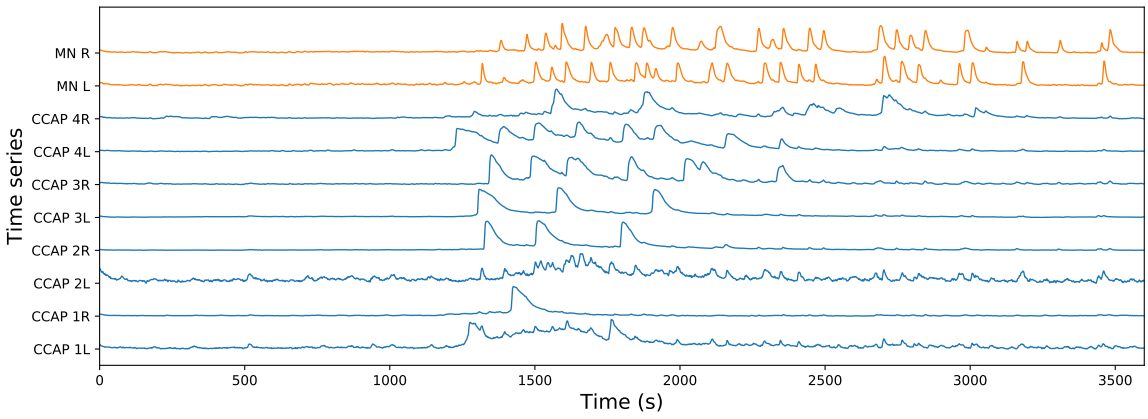

Figure 14. Example of poor temporal match between α CCAP neurons and motoneurons. Example of an experiment with a poor temporal match during the post-ecdysis phase as very few α CCAP neurons increased their activity during motoneuronal oscillations. "MN" and "CCAP" indicate motoneurons and α CCAP neurons respectively. The letter indicates the side (left/right), while the number indicates the abdominal segment of the neurons.

3.2 Models

3.2.1 Logistic model

After finding that CCAP neurons are functionally coupled to the motoneurons, I built a model that would allow me to better understand the relationship between these two populations of neurons. I wanted to know if all neurons affected the motoneurons in the same way, and also how well the activity of the α CCAP neurons could predict the motoneuronal oscillatory state.

The model that takes the activity of α CCAP neurons as input and generates the motoneuronal oscillatory activity as output. As the amplitude of the motoneuron oscillations does not appear to be regulated by α CCAP neurons, I employed the same binary signal used to compute the initiation of the motoneuronal activity (Figure 13c) to describe the oscillatory and non-oscillatory motoneuronal activity. The motoneuron oscillation generator (CPG) integrates the signals from AN1-AN4 α CCAP neurons and produces a probabilistic oscillatory response.

The system was modeled as a logistic regression:

$$p(t) = \frac{1}{1 + \exp\left(-\beta - \sum_{i=1}^{8} w_i f_i(t)\right)} \tag{13}$$

Where $p(t)$ represents the model probability of motoneurons to oscillate at time t, $f_i(t)$ the i-th α CCAP neuron time series, w_i the i-th α CCAP neuron weight and β the offset.

As an alternative, I also fitted a single weight model (same value for all w_i), based on the assumption that all α CCAP neurons affect the motoneuronal activity in the same way. The model coefficients were estimated using the maximum likelihood estimation (MLE) with the constraint that all weights must be positive, as I showed that an increase of the α CCAP neuronal activity is associated with a higher motoneuronal oscillatory probability.

The fittings showed that the maximum likelihood was reached without the need of every α CCAP neuron time series of an experiment, as it can be seen in Figure 15a, b; or said differently, the maximum likelihood solution had weights set to zero. The minimum number of α CCAP neurons required to reach the maximum likelihood was 2, the maximum was 6 and the average was ∼4. These results should not be interpreted to mean that some α CCAP neurons did not have any effect in the motoneuronal oscillatory activity; I expect all of them to have an effect, but some may not contribute to the further maximization of the likelihood of the model to generate the observed oscillatory activity pattern. Reasons for that could be activity redundancy, low SNR, which could be caused by different factors, or simply the stochastic nature of the neural ensemble. The weights were also highly variable, which could be seen as an indicator of the degeneracy of the system, as it shows that α CCAP neurons with diverse activity dynamics still generate similar motoneuronal activity (Edelman and Gally 2001; Whitacre 2010; Whitacre and Bender 2010).

It can be seen in Figure 15a, b that during the motoneuronal oscillatory activity, $p(t)$ increases accordingly; one exception can be observed in Figure 15b, where the $p(t)$ barely increases during the

rare post-ecdysis oscillatory events. The cause of this is the lack of significant increments of the activity of the α CCAP neurons during these events.

One way to visualize the quality of the fitting is to compute the classification error rate (CER), or the proportion of misclassified cases. To do so, I first binarized the $p(t)$ of the single- and multi-weight fittings with the following equation:

$$b(t) = \begin{cases} 1, & \text{if } p(t) \geq x \\ 0, & \text{if } p(t) < x \end{cases} \tag{14}$$

The $p(t)$ functions were binarized ($b(t)$) with a threshold (x) of 0.5 and with a value optimized to minimize the CER of the fitting (Figure 15c, Table 13). As an alternative approach, I compared them to a basal CER, which is the CER obtained using the assumption that no oscillations occur during the entire experiment. As expected the CER of the multi-weight model was lower than the single-weight model with either unoptimized or optimized thresholds, with the exception of a single experiment, where the optimized single-weight CER was marginally lower than its optimized multi-weight counterpart. The reason for this is that the model is probabilistic and the fitting maximizes the likelihood, not the accuracy of a binarized probability function. The optimized single- and multi-weight models reduced the basal CER by a mean of ∼56 % and ∼64 % respectively.

A different approach to measure the performance of the single- and multi-weight models is to compute the area under the curve (AUC) of receiver operating characteristic (ROC) curves. ROC curves have the advantage of showing the relationship between the TPR, or proportion of positives that are correctly identified as such, and the FPR, or proportion of negatives that are wrongly identified as such, when varying the threshold during the binarization. Different threshold values give different levels of TPR and FPR: a high threshold is less likely to produce a false positive (FP) (false prediction of oscillations) but more likely to produce a false negative (FN) (false prediction of no-oscillations), while a low threshold is less likely to produce a FN but more likely to produce FP. The ROC curve gives a picture of the whole spectrum of such tradeoffs. I compared the AUC of the single- and multi-weight models, and in all experiments except one (Figure 16a), the multi-weight AUC values were closer to 1 (a perfect classifier) (Figure 16b, Table 14). The reason for the single-weight model performing better in one experiment, was because the objective function was not the maximization of the AUC. The single- and multi-weight models both performed very well at classifying the state of the motoneurons with an AUC mean of 0.922 and 0.939 respectively.

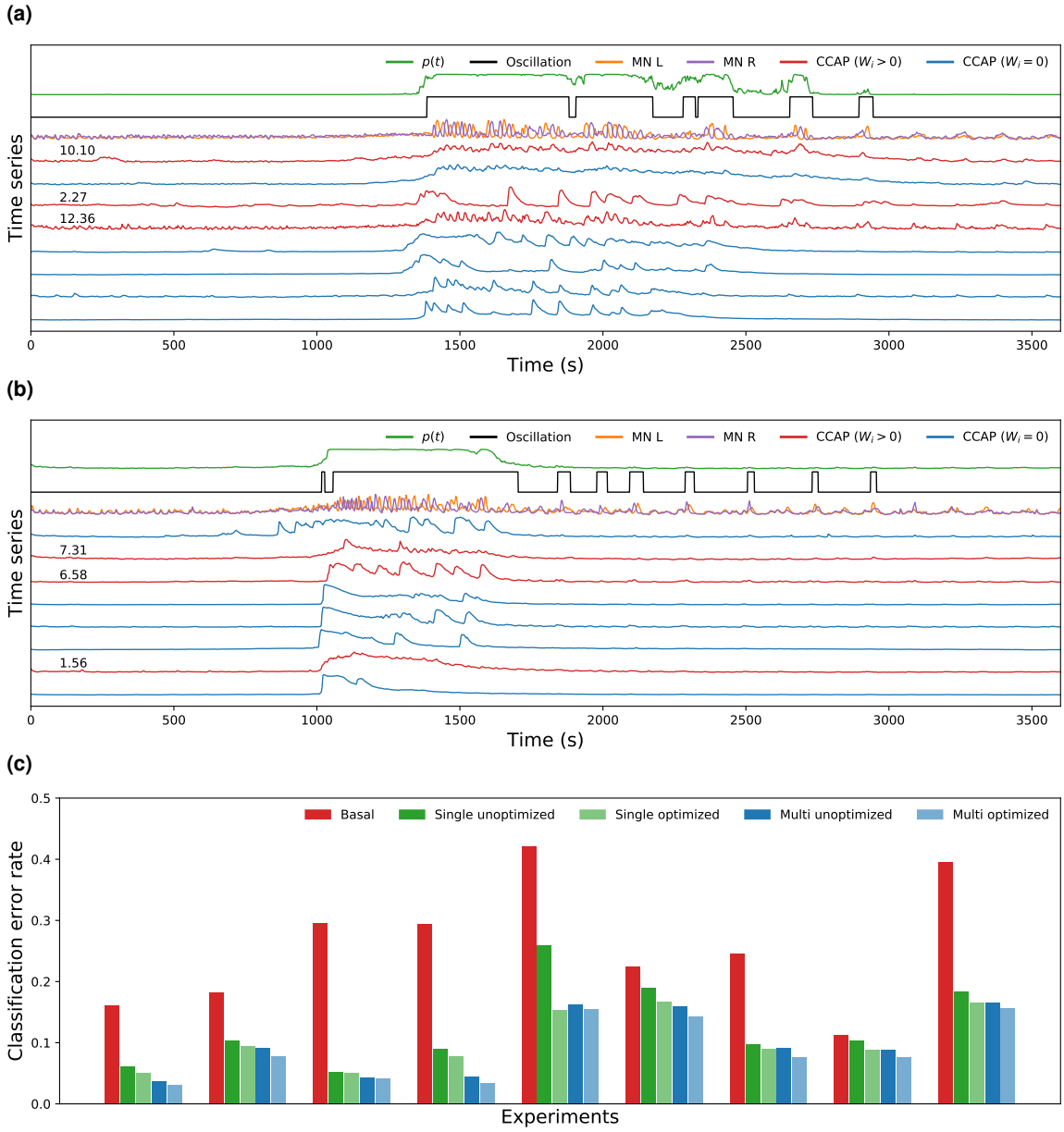

Figure 15. Logistic model. **(a)**, **(b)** Time series of α CCAP neurons with their corresponding weight value if it is positive ("CCAP $(W_i > 0)$"), or no value if it is zero ("CCAP $(W_i = 0)$"). All weight values were computed through multi-weight model fitting. Left ("MN L") and right ("MN R") motoneurons, the binarized oscillatory activity ("Oscillation") and the model probability of oscillation $(p(t))$ are displayed to show the quality of the fitting. **(a)** shows a good match between the model $p(t)$ and oscillatory state of the motoneurons, while **(b)** shows a bad match during the post-ecdysis phase, as result of the lack of α CCAP simultaneous activity. **(c)** Logistic model CER. Contrasts the basal (assumption that motoneurons never oscillate) CER against single- (green tones) and multi-weight (blue tones) fittings. The unoptimized CER is obtained by setting the $p(t)$ threshold to 0.5, while the optimized one, uses the threshold that returns the lowest CER.

	Experiment										
	1	2	3	4	5	6	7	8	9	Mean	SEM
Basal	0.162	0.182	0.296	0.295	0.421	0.224	0.246	0.113	0.396	0.259	0.034
Single unoptimized	0.062	0.103	0.053	0.090	0.259	0.190	0.098	0.104	0.184	0.127	0.023
Single optimized	0.051	0.095	0.051	0.078	0.154	0.168	0.091	0.088	0.165	0.104	0.015
Multi unoptimized	0.038	0.092	0.044	0.045	0.162	0.160	0.092	0.088	0.166	0.098	0.018
Multi optimized	0.031	0.078	0.041	0.035	0.155	0.143	0.076	0.076	0.157	0.088	0.017

Table 13. Logistic model CER. Values of Figure 15c.

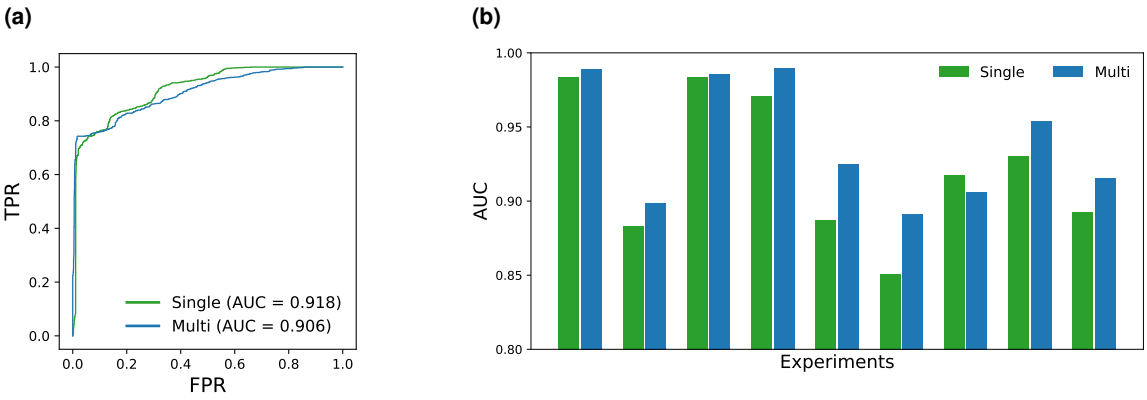

Figure 16. ROC curve analysis. (a). ROC curve sample (from Figure 15b). **(b)** AUC values of single- and multi-weight fittings.

	Experiment										
	1	2	3	4	5	6	7	8	9	Mean	SEM
Single	0.984	0.883	0.984	0.971	0.887	0.851	0.918	0.931	0.893	0.922	0.016
Multi	0.989	0.899	0.986	0.990	0.925	0.891	0.906	0.954	0.915	0.939	0.014

Table 14. Area under curve. AUC values of Figure 16b.

Higher complexity models tend to fit the data better than simpler ones, so it was not surprising that the multi-weight model performed better than the single-weight one. To select the best model by taking into account the tradeoff between the goodness of the fit and the complexity of the model I used the akaike information criterion (AIC) (Akaike 1974). For all 9 experiments the multi-weight model performed notoriously better (its values were lower) than the single-weight model (Table 15).

	Experiment								
	1	2	3	4	5	6	7	8	9
Single	908	1803	1092	1519	3714	2976	2312	1489	3108
Multi	711	1598	888	891	2481	2464	2019	1227	2675

Table 15. Akaike information criterion. AIC values of single- and multi-weight model fittings of every experiment.

At first sight it could be argued that all α CCAP neurons should affect the motoneuronal activity in the same way, thus making the single-weight model a more biologically sound model. For this to be true, a couple of requirements would need to be met, which can be divided into biological and experimental ones. Some possible requirements are presented below:

Biological requirements:

- The concentration of the calcium dye are roughly equal in all α CCAP neurons, and the level of fluorescence of α CCAP neurons determines their concentration of intracellular calcium, or said differently, two α CCAP neurons with the same level of fluorescence must have roughly the same concentration of intracellular calcium.
- The intracellular calcium determines the level of activity (and peptide release rate) of α CCAP neurons.
- The CPG response depends only on the level of activity of α CCAP neurons, and all exert the same level of influence on the CPG.

Experimental requirements:

- The neuronal circuit is not damaged during the preparation and recording of the experiment.
- Accurate identification of the α CCAP neurons.
- SNR of all α CCAP neurons is roughly similar during the entire recording.

The multi-weight model treats each α CCAP neuron differently by assigning different weights to each, and in this way is able to compensate for the non-uniformities of either biological or experimental origin. In this model, α CCAP time series with a lower predictive power of the motoneuronal oscillatory state are either discarded or assigned low weight values. As the predictive power of the α CCAP neurons varies considerably, since the requirements are not completely met, the multi-weight model surpasses the single-weight model in terms of quality, according to AIC.

3.2.2 Conductance-based model

The logistic model, as it was shown, is an abstract model capable of fitting a probability function to a binary motoneuron oscillation time series, but incapable of modeling the calcium dynamics. To get a deeper insight on the dynamics of the neuronal ensemble, I looked for a less abstract model that could generate the observed calcium dynamics.

Given the lack of a structural description of the circuit and following the Occam's razor principle, I looked for a simple conductance-based bursting CPG model that I could use as a starting point to model the calcium dynamics. One model that met my needs was developed by Jalil et al. 2010 and is based on Shilnikov and Cymbalyuk 2005. The model uses two fast non-delayed reciprocally inhibiting endogenously bursting neurons that synchronize in antiphase.

I adapted the model to generate fluorescence (calcium) spikes during the motoneuronal oscillation phase that matched the motoneuronal activity pattern of the 9 experimental recordings (Methods, section 2.6). More specifically I tried to match the oscillation timing, the calcium interspike interval (ISI), the spike phase difference and the time constant of each experiment.

The adapted model is made of 10 neurons, 8 α CCAP neurons and 2 motoneurons (Figure 17). Each α CCAP neuron releases a peptidergic signal that depolarizes the motoneurons, causing them to oscillate. α CCAP neurons release the signal according to their fluorescence time series factored by a weight (already computed in the logistic model). Motoneurons are mutually inhibitory and oscillate in antiphase with a frequency dependent of the strength of the peptidergic signal.

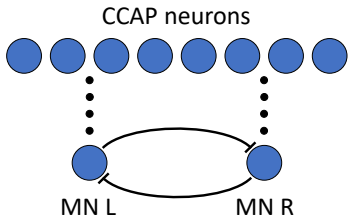

Figure 17. Circuit structure. Top blue circles represent the 8 α CCAP neurons that release the peptidergic signal (black circles) that activate the oscillatory behavior of the reciprocally inhibiting motoneurons.

Before adjusting the parameters of the model, I characterized a few more properties of the experimental motoneuronal dynamics, besides the already computed main oscillation period (Figure 7b, Table 6).

I used the derivative in time of the motoneuron time series during the ecdysis phase to estimate the bursting duty cycle by dividing the fluorescence increasing interval of the spike by the ISI. I noticed that there was an apparent high variability (within each experiment) that also significantly changed depending on the measurement method, so I estimated by visual inspection that the duty cycle was $\sim$20 %.

To compute the fluorescence time constant of the motoneurons, I fitted an exponential decay function template to the time series segments that displayed a clear exponential decay, and extracted the time constants of the fitted function templates (Methods, section 2.7). For every experiment its segment time constants were averaged and assigned to the τ_f parameter of the model (Figure 18, Table 16).

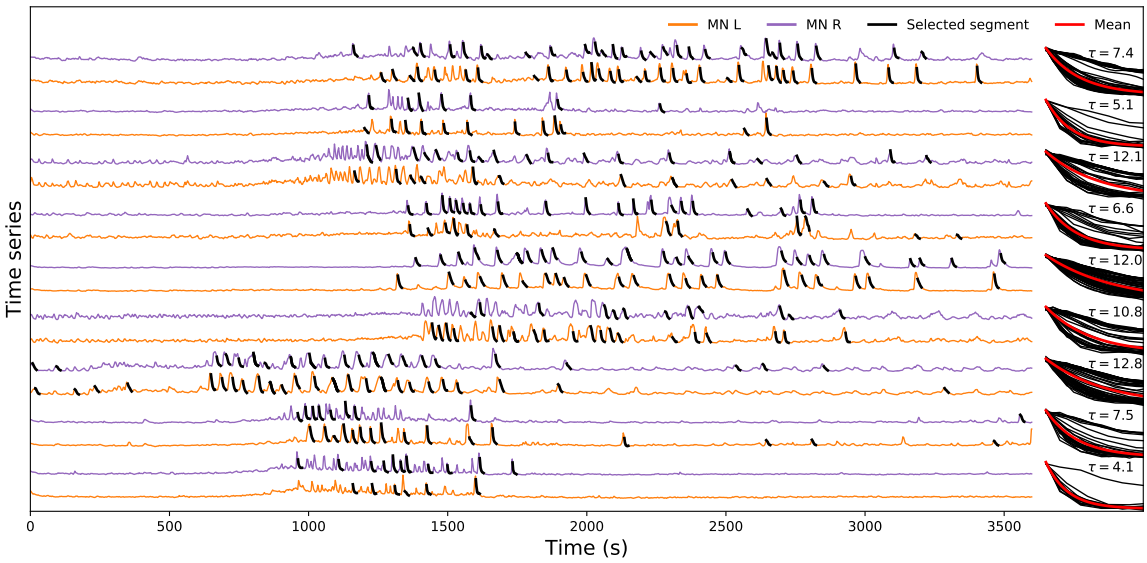

Figure 18. Motoneuron time constants. Left side of the plot shows the left ("MN L") and right ("MN R") motoneuron region time series for 9 experiments with the selected exponential decay segments marked in black. At the right side, same segments are plotted overlapped of each other, including their mean exponential decay and its τ value.

	Experiment								
	1	2	3	4	5	6	7	8	9
Mean	4.1	7.5	12.8	10.8	12.0	6.6	12.1	5.1	7.4
SEM	1.0	1.3	0.9	1.2	0.7	1.0	1.2	1.0	0.8

Table 16. Motoneuron exponential decay time constants. Time constant (s) values of Figure 18.

I fitted the model in multiple passes of manual parameter adjustments and simulation sessions. I initially tried to roughly match the calcium ISI to 40 s and the duty cycle to 20 %. This was accomplished by manually adjusting τ_{K}, τ_{Na}, g_{K}, g_{L}, g_{Syn}, g_{CCAP}, V_{Shift} and σ_{X} parameters of a noiseless model (without equation 6g and its associated current). This process was especially difficult as most parameters have multiple effects on the model dynamics so that adjusting a particular parameter to match one aspect of the dynamics could affect the match of a different one. The initial model (Jalil et al. 2010) oscillated spontaneously so parameters also had to be fitted so that the model oscillated when $p(t)$ = 1 (CCAP neurons peptidergic output is at its maximum), but not when $p(t)$ = 0 (when it is at its minimum). Once I found the parameter values to get a rough approximation of the target dynamics, I added noise to the model (equation 6g) to generate spike phase noise (as seen in Figure 11). To more accurately fit the model, I studied the effect that each parameter has on the dynamics near the vicinity of the rough model approximation and fitted the parameters accordingly.

The resulting fitted parameter values were identical for all experiments except for τ_{f} and τ_{K}, which were used to fit the exponential decay and period, respectively (Table 17).The exponential decay could only be fitted through the τf parameter, and does not affect the model dynamics, as it is used only to produce the fluorescence (calcium) output. The period, in contrast, is affected by many parameters, but τK affects it linearly and does not affect the duty cycle and phase difference (as it will be shown below), making it much easier to adjust manually.

An example of the output of the model is shown Figure 19, where the motoneuron fluorescence and voltage are plotted next to each other for comparison. The temporal magnification shows that during the bursting phase the fluorescence, increases, and decreases during non-bursting phase (in both cases, with a τ_f time constant).

		Experiment								
Parameter	Unit	1	2	3	4	5	6	7	8	9
C	nF	0.5	”	”	”	”	”	”	”	”
τ_{Na}	s	0.055	”	”	”	”	”	”	”	”
τ_{K}	s	55.2	63.9	125.6	67.7	136.5	71.5	71.5	69.0	88.1
τ_{f}	s	3.2	4.1	11.2	10.0	11.2	4.8	8.6	3.7	4.4
g_{Na}	nS	200	”	”	”	”	”	”	”	”
g_{K}	nS	45	”	”	”	”	”	”	”	”
g_{L}	nS	10	”	”	”	”	”	”	”	”
g_{Syn}	nS	0.5	”	”	”	”	”	”	”	”
g_{CCAP}	nS	1	”	”	”	”	”	”	”	”
E_{Na}	V	0.045	”	”	”	”	”	”	”	”
E_{K}	V	−0.070	”	”	”	”	”	”	”	”
E_{L}	V	−0.046	”	”	”	”	”	”	”	”
E_{Syn}	V	−0.0625	”	”	”	”	”	”	”	”
E_{CCAP}	V	0	”	”	”	”	”	”	”	”
V_{Shift}	V	0.022	”	”	”	”	”	”	”	”
τ_{X}	s	0.001	”	”	”	”	”	”	”	”
σ_{X}	nA	0.03	”	”	”	”	”	”	”	”

Table 17. Conductance model parameters. Parameter values used, except for τ_{K} and τ_{f}, were identical for every experiment simulation.

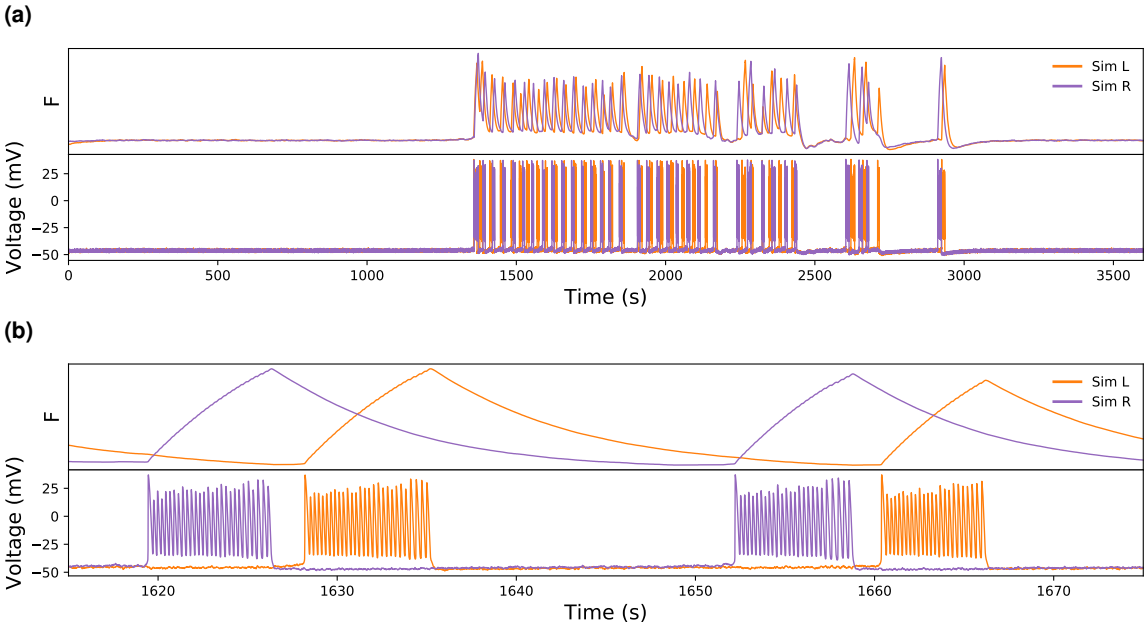

Figure 19. Simulation of fluorescence spikes. (a, b) Plots showing at the top and bottom, the simulation fluorescence and voltage time series, respectively, of left (“Sim L”) and right (“Sim R”) motoneurons. **(a)** shows the complete experimental simulation, while **(b)** shows a small temporal segment of **(a)**.

Two examples of the output of the model compared to the experimental data can be seen in Figure 20a, b. α CCAP neurons peptidergic outputs are multiplied by weights, summed and transformed with a logistic function to generate the gating variable $p(t)$. In this way, through $p(t)$, α CCAP neurons modulate the oscillatory behavior of the motoneurons.

The timing of the simulation oscillations approximately matched that of the experiments, even during the periods of lower spiking frequency, as it can be seen in Figure 20b. This is especially interesting considering that $p(t)$ was fitted to a binarized (as opposed to graded) motoneuronal activity signal. Another noteworthy effect is that, as more time passes since the last oscillation, the neurons are more likely to begin oscillating again. This effect is the result of slow Potassium dynamics that slowly stop inhibiting APs; this can be seen in the last oscillation period in Figure 20a. Figure 20b shows spike FPs during the pre-ecdysis phase, which are caused by $p(t)$ not being close enough to 0 during that phase. One way to solve this problem, could be by doing a weighted logistic fitting (MLE) and giving the pre-ecdysis phase a higher weight; in this way $p(t)$ would become closer to 0 during the pre-ecdysis.

It can be observed that the simulation spike frequency and its exponential decay match that of the experiments, as they were fitted through the τ_{Na} and τ_f parameters. The noise caused by equation 6g adds amplitude and phase variability which resembles the one observed from the experiments.

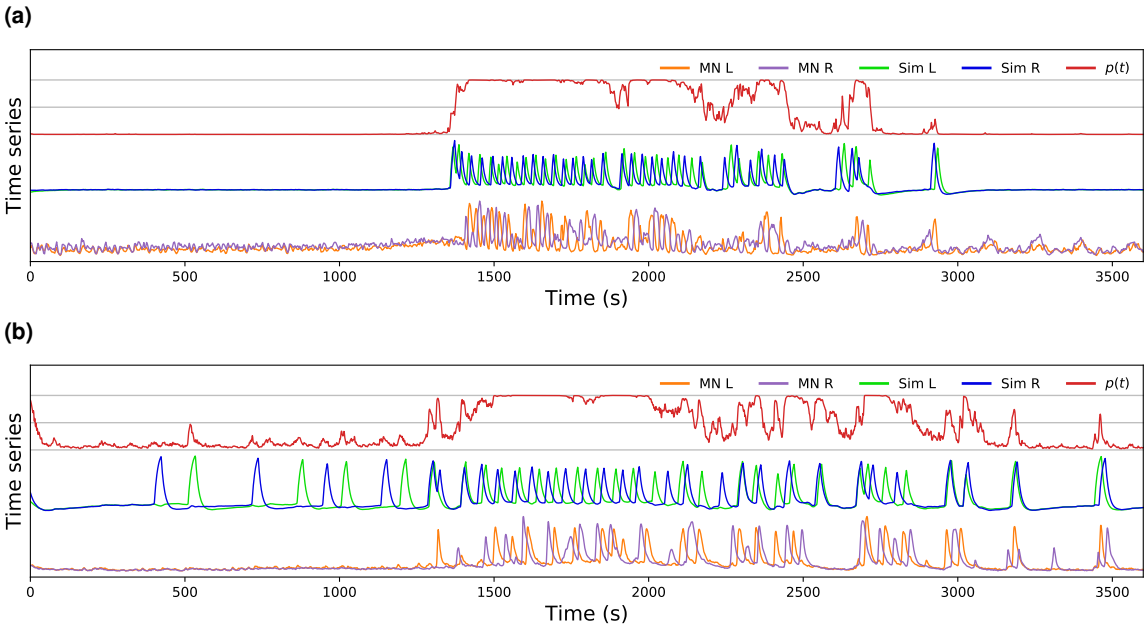

Figure 20. Simulation samples. (a, b) Samples of a simulation of two different experiments. The gray grid mark the probabilities 0, 0.5 and 1. "MN L", "MN R", "Sim L" and "Sim R" indicate the left and right experimental, and left and right simulated motoneurons respectively. $p(t)$ indicates the probability of oscillation.

The effect of the stochasticity in the simulation can be observed in Figure 21 in the time domain (a) and time-frequency domain (b), with the bottom plot showing the experimental data. The same parameters were used to perform 3 simulations, and, as can be seen, the current noise caused spike jittering, amplitude variability, and stochastic spike generation. The scaleograms show a high similitude between the simulations and the experimental activity in terms of their oscillation timing and frequency.

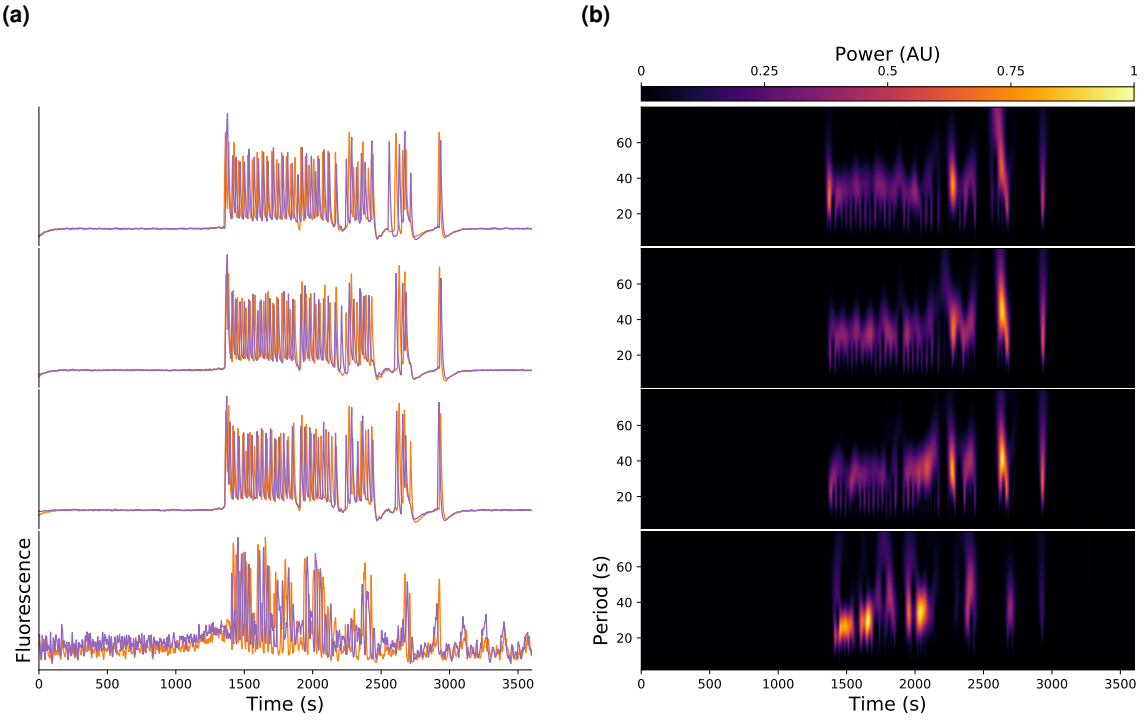

Figure 21. Simulation stochasticity. Three different simulations using the same parameters show the variability caused by the stochasticity of the model in the time domain **(a)** and in the time-frequency domain **(b)**. Bottom row shows the experimental data for comparison purpose.

Figure 22 compares simulated and experimental motoneuron time series of 9 different experiments in the time and time-frequency domain. As can be seen, some simulations suffer from pre-ecdysis spikes, but still do a good job at temporally matching the periods of oscillation. Each plot in the time domain has its corresponding plot in the time-frequency domain; each pair shows at the bottom the experimental and at the top the simulated data. To reduce the noise of the model scaleogram, each simulation was repeated 10 times and their scaleogram averaged. In all experiments the simulations showed a good time-frequency match to the experimental data.

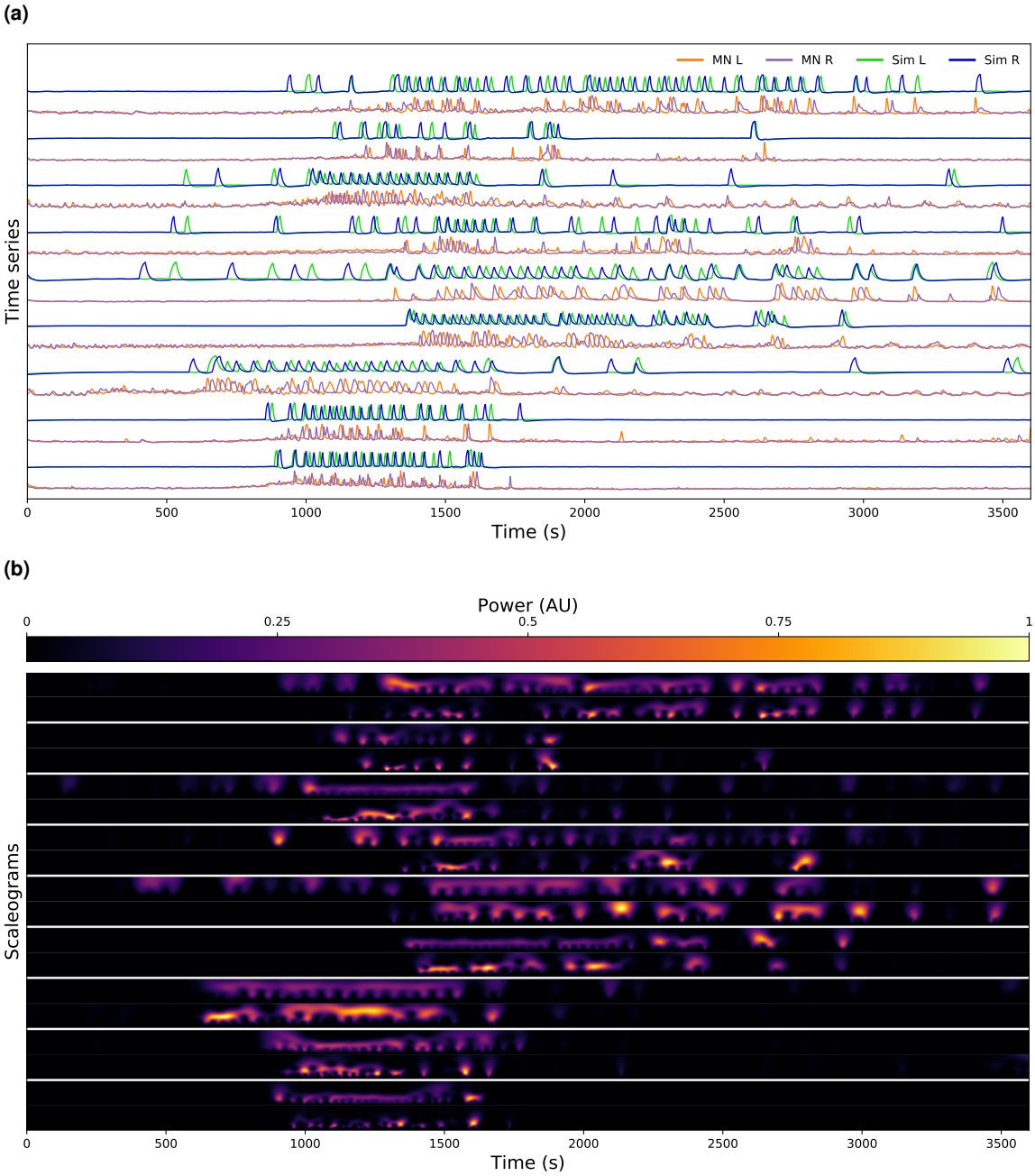

Figure 22. Simulations. Analog to Figure 21 **(a)** shows experimental and a simulation time series of 9 experiments. “MN L”, “MN R”, “Sim L” and “Sim R” indicate the left and right experimental, and left and right simulated motoneurons respectively. **(b)** shows their corresponding scaleograms, except that the simulation scaleograms are the average of 10 simulations. Each row shows at the bottom and top the experimental and simulated motoneurons respectively.

Even though there is no connectivity description of the circuit, let alone an electrophysiological description of the neurons involved, I was able to adapt a simple conductance-based model to simulate many of the activity pattern features observed in the experimental recordings. The model and the fitting process should be easy to adapt to an updated model, once newer details of the circuit structure and dynamics are discovered.

3.2.3 Parameter sensitivity

The effect of the fitted parameters (τ_K, τ_{Na}, g_K, g_L, g_{Syn}, V_{Shift} and σ_X) was studied near the point, in the parameter space, of the solution (Table 17). For each studied parameter, multiple simulations were run at a slightly different parameter value; the period, duty cycle and phase difference were then computed for each simulation (Methods, section 2.8). I generated 2D scatter plots of the relationship between each studied parameter and then measured dynamics properties. These plots were then used to check the effect of each parameter in the vicinity of the solution (Figure 23).

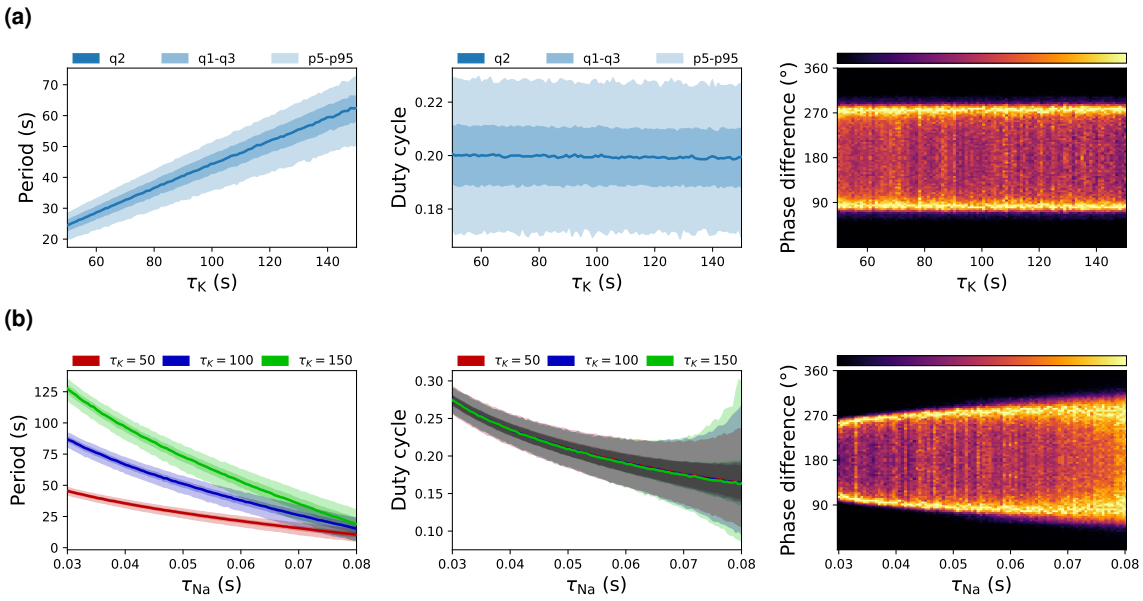

Figure 23. Effect of the parameters in the model dynamics. Effect of the modification of τ_k, τ_{Na}, g_K, g_L, g_{Syn}, V_{Shift} and τ_X parameters in the vicinity of the solution. The first column shows the period, the second, the duty cycle and the third, the phase difference at varying parameter values. The period and duty cycle show in highly saturated color the median, in less saturated color the q1-q3 range, and in the least saturated color the p5-p95 range. Starting at the second row, the plots show the effect of the parameters at different τ_k values for the first and second column, and at τ_k = 100 s for the third column. The third column shows the phase difference probability distribution function (PDF) at every parameter value. Statistics for every parameter combination were obtained through simulations of 50 000 s with a $p(t)$ = 1.

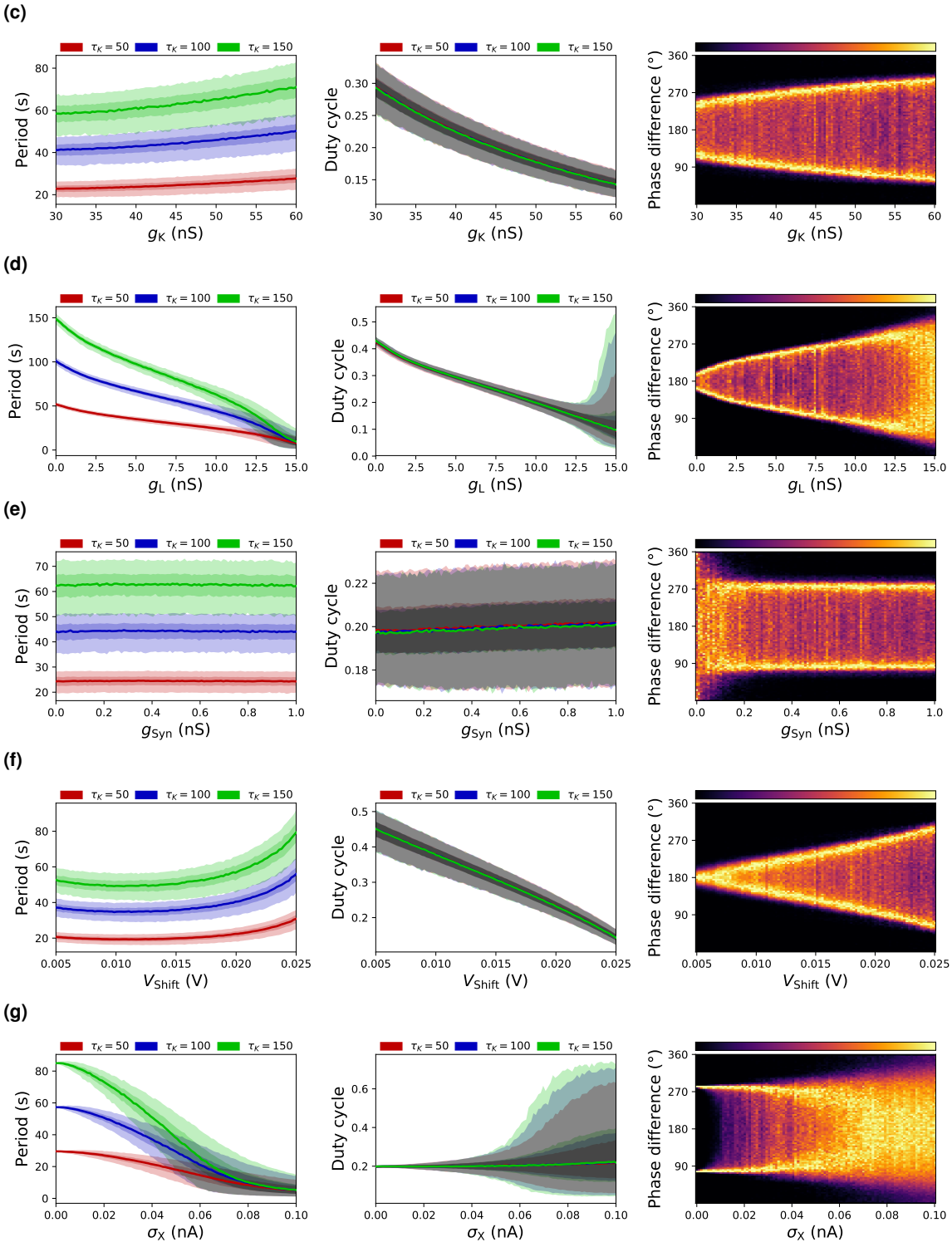

Figure 23 (continued). Effect of the parameters in the model dynamics.

I found that τ_K affected the period in a very linear positively correlated way, but did not significantly affect the duty cycle and phase difference (Figure 23a). The high specificity of the τ_K parameter made it ideal to fit the model period so that it generated oscillations at each specific motoneuronal period (Table 6) whenever $p(t) = 1$.

The effects of the other parameters on the model were studied at τ_K = 50 s, 100 s and 150 s, to assess any possible differential effect that the parameters may have on the model at different τ_K values. The phase difference plots on the other hand, show the phase noise at τ_K = 100 s.

τ_{Na} shows a negative correlation to the period and duty cycle, and shows an increased duty cycle dispersion at high parameter values as result of the current noise (Figure 23b). The current noise (equation 6g) also reduces the preference for a neuron to initiate its bursting activity immediately after its counterpart stops bursting, which can be seen in the phase difference plot as a more uniform PDF at higher parameter values. The dark areas in the plot also show that the mutual inhibition does not allow the neurons to burst at the same time.

g_K is positively correlated to the period and negatively correlated to the duty cycle, it has a minor effect in the period, but a greater effect in the duty cycle (Figure 23c). τ_K does not seem to have any effect in the duty cycle and the phase difference plot shows a U-shape PDF in the whole probed parameter space.

The effect of modifying the g_L parameter has similarities to the modification of τ_{Na} (Figure 23d). Both are negatively correlated to the period and duty cycle, and at increasing parameter values the duty cycle dispersion increases as result of the current noise, which also makes the PDF more uniform.

The parameter g_{Syn}, as expected, does not have any significant effect on the period and duty cycle (Figure 23e). At values lower than $\sim$0.05 nS the neurons oscillate independently without a preference for alternated bursting activity. In the $\sim$0.05 nS to $\sim$0.15 nS range there is a visible preference for non-overlapping bursting activity, and the phase difference preference shows uniformity in the non-overlapping interval. At higher parameter values the overlapping probability is reduced and the PDF takes the U-shape.

V_{Shift} produces an accelerating period increase at both sides of the local minimum at $\sim$12 mV (Figure 23f). The duty cycle decreases linearly at increasing values of the parameter and also reduces its dispersion. The phase difference plot shows a uniform non-overlapping burst PDF that takes a U-shape form at values greater than 7 mV.

The σ_X parameter controls the amount of current noise. At low values (< ∼5 pA) it does not affect the period, whereas at greater values it reduces it by helping neurons reach the AP voltage threshold (Figure 23g). At higher values, spontaneous AP occur with higher frequency and at some point (> ∼80 pA) the τ_K parameter does not have any differentiating effect on the period. The mean duty cycle only increases slightly at higher σ_X values, in contrast, the dispersion increases notoriously with a clear skew towards high duty cycle values. At low noise levels the phase difference plot shows a U-shaped PDF with only two possible phase difference values, at higher noise levels it mutates into a more uniform and higher overlapping probability PDF.

As $p(t)$ is a gating variable, but also the probability of motoneurons being in oscillatory state (equation 13), its value should ideally be inversely proportional to the oscillatory period. I plotted the product of a constant $p(t)$ and the resulting period, and found that $p(t)$ and the period behaved roughly in an inversely proportional way, as their product stayed relatively constant (Figure 24a)

$p(t)$ does not completely work as an independent probability, since after a calcium spike ends, follow-up spikes have difficulty initiating immediately, because of the refractory period. $p(t)$ affects the refractory period, the higher its value, the shorter the refractory period. Equation 6g introduces stochasticity to the system and adds jitter to the spike timing making it behave more randomly, while maintaining the inverse proportionality. In summary, $p(t)$ acts as an oscillation probability variable in many aspects, except those that would make the model nonphysiological. Figure 24b shows the oscillatory behavior at four different constant $p(t)$ values (0.25, 0.5, 0.75 and 1).

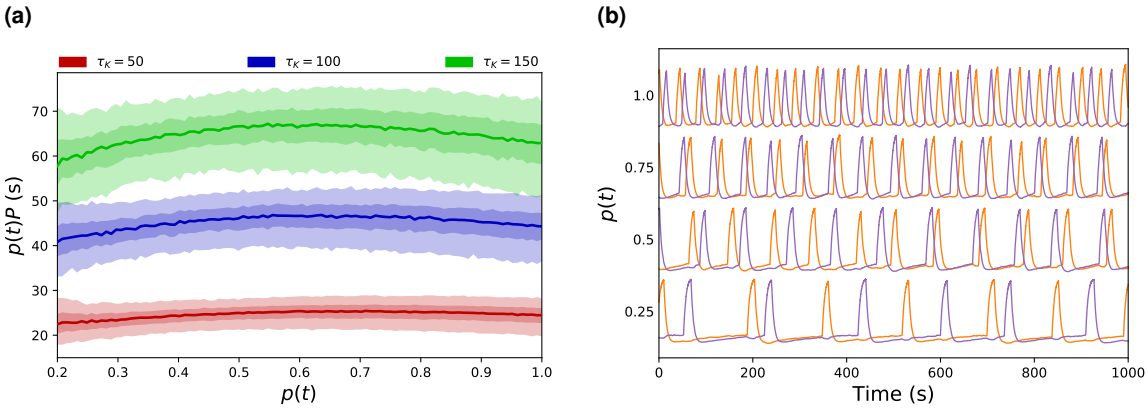

Figure 24. Inverse proportionality of $p(t)$ and the period. (a) Plot of the effect in the $p(t)P$ ($p(t)$ multiplied by the period (P)) when holding $p(t)$ at different constant values from 0.2 to 1. The color saturation has the same meaning than in Figure 23. **(b)** Model motoneuronal calcium time series at different constant values of $p(t)$ (0.25, 0.5, 0.75 and 1).

The conductance-based model was fitted by adjusting its parameters to match the metrics computed from the experimental data. Some parameters affected only one metric of the model, while others affected multiple. Of all the metrics I tried to match, the duty cycle could not be affected by a single parameter without affecting other metrics. As the model was fitted manually, it was easier to fit it to match the duty cycle before the period and phase noise, since the last two could be matched through single parameters without affecting other metrics.

Of course, the parameter solutions that I found are not the only ones that are possible, but they were easy to find through manual adjustment of the parameters. An alternative could have been to do the parameter adjustment automatically through optimization algorithms such as genetic algorithms, but this was not attempted as it was not necessary to fit the experimental data.

3.3 Behavior

One question that arises when studying highly manipulated systems, is how much of the measured phenomena occurs in the intact animal: is the neural activity observed in the *ex vivo* preparation the same as that which generates the observed *in vivo* motor patterns? To contrast the *ex vivo* activity to the *in vivo* activity, I analyzed the pupal motor behavior of intact animals removed from their puparium. I developed computational methods to quantify different aspect of the ecdysis motor programs in the puparium-free preparations to contrast them to the calcium motoneuronal activity, which is my third and last proposed objective of the thesis. The analytic process is divided into three phases, the computation of the position of midline of the pupa, the generation of the time-space diagram, and its quantification.

To compute the midline of the pupa, a sequence of image processing operations was applied to every frame of the video. Color (RGB) frames were extracted from the video sequence in real number format, with 0 and 1 representing the minimum and maximum intensity, respectively (Figure 25a). The images were converted to grayscale by averaging the intensity of the three color component channels (Figure 25b). Pixels of the images were thresholded by setting them to 0 if the grayscale valued were lower than 0.1 or to 1.0 otherwise (Figure 25c). Holes, or black regions inside white regions were filled (Figure 25d). The threshold value was chosen arbitrarily, but I found that the resulting thresholded image was not very sensitive to the exact value. To extract the main behavioral features, high spatial frequency details were removed in a two-phase process. The images were convolved with a gaussian function with σ = 3 pixels (Figure 25e) and then thresholded at a threshold of 0.5, to avoid expanding (dilating) or reducing (eroding) the borders of the pupa (Figure 25f). Regions with less than 10 000

white pixels, roughly 20 % of the area of the pupa seen in the figure, were discarded (Figure 25g). The left- and rightmost pixels of the pupa along the anteroposterior axis were then computed. The average between the left- and rightmost pixels along the axis were considered to represent the midline of the pupa (Figure 25h).

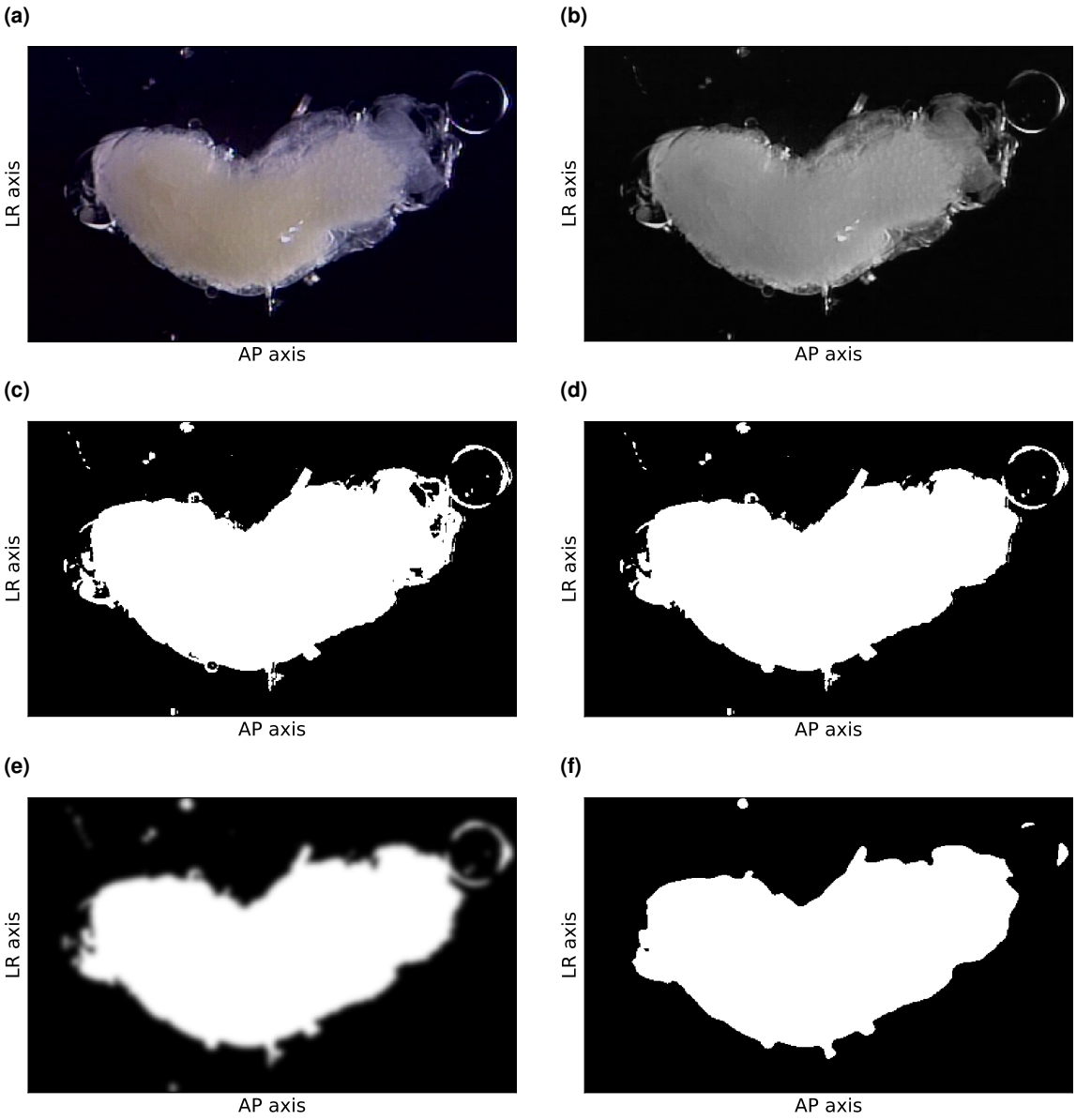

Figure 25. Midline computation. Sequence of image processing steps used to compute the midline of the pupa for every frame of the video. The "AP axis" and "LR axis" indicate the anteroposterior and left-right axis respectively. An RGB video frame is extracted **(a)** and converted to a grayscale image **(b)**, then thresholded **(c)** and its black holes filled **(d)**. Blob borders are softened by applying a gaussian filter **(e)** and thresholding again **(f)**.

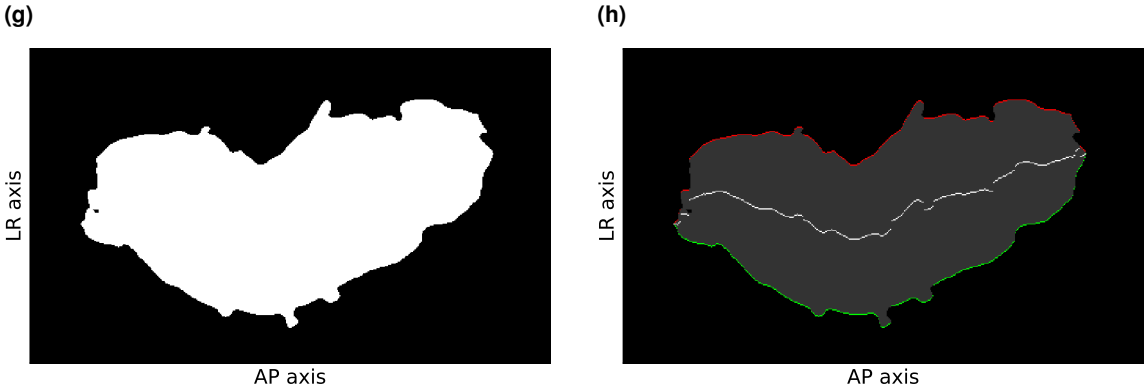

Figure 25 (continued). Midline computation. Small blobs are discarded **(g)** and the left (green) and right(red) borders are computed **(h)**. The mean of the two borders represents the midline (white).

The varying position of the midline was used to generate a time-space diagram, which showed a distinctive pattern for each major motor pattern (Figure 26a). The color of the diagram indicates the position in the left-right axis of the midline along the anteroposterior axis. Discontinuities and abrupt color changes of the top time-space diagram indicate sudden movement of the pupa along the anteroposterior and left-right axis respectively, caused by vibration of the microscope table. I reduced these artifacts in the mid diagram in a two-step process by centering the pupa along the anteroposterior axis and cancelling the fast movement of the midline along the left-right axis when it surpassed an arbitrary threshold. I did not try to reduce artifacts caused by overexposure of the microscope camera or the removal of the pupa from the viewing field during the experimental recording, both of which were rare events and had minor impact in posterior analyses. The bottom time-space diagram shows the mid section of the mid diagram, this section represents the mid section of the midline and is very sensitive to the swinging motor pattern. For easier visualization of the mid section left-right position I generated a time-series out of it by taking the average left-right position of the mid section (Figure 26b).

An inset of the middle diagram showing the different motor patterns is shown in Figure 27. The anteroposterior axis is oriented with the top of the diagram pointing to the anterior side of the pupa. As the peristaltic motor activity begins in the anterior and propagates to the posterior region of the animal, it generates a descending line pattern in the diagram. The swinging motor pattern is characterized by a great color variation in the anteroposterior mid section and a lengthening and shortening of the diagram across the anteroposterior axis. The lengthening occurs when the pupa is straight and the shortening when it bends. Another noticeable feature of the pattern is that the bending tends to propagate from the anterior to the posterior region, producing a descending diagonal line. The stretch-compression motor pattern is characterized by a lengthening and shortening of the midline with minor changes in its left-right position.

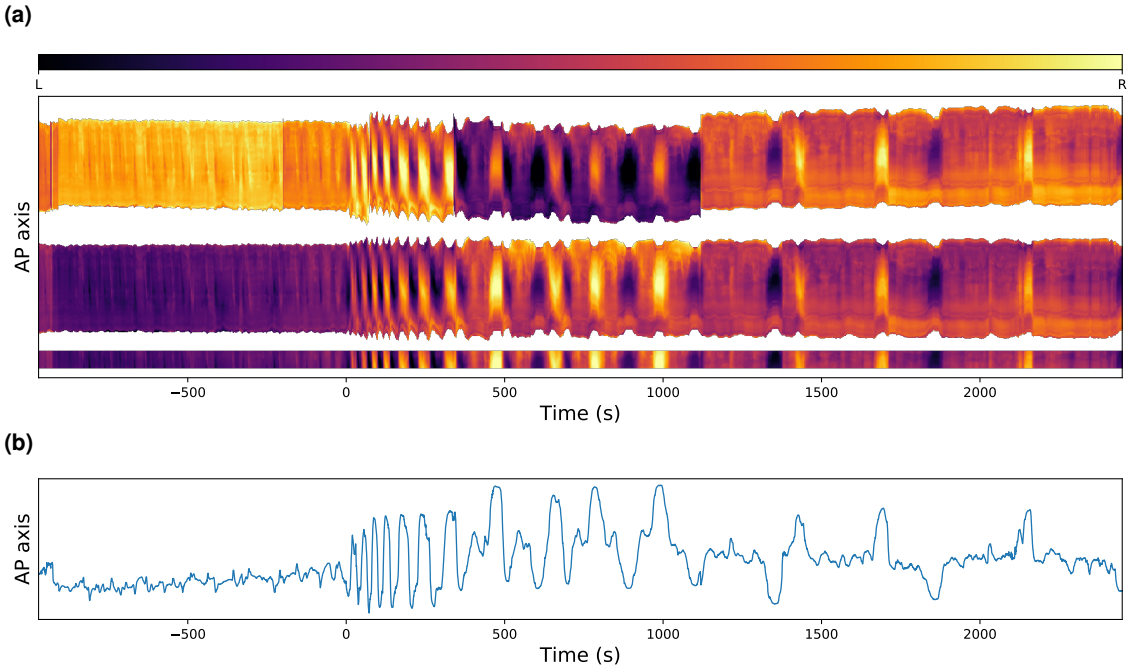

Figure 26. Computation of the behavior time-space diagram. (a) time-space diagrams generated from the midline position, computed for each video frame. The color indicates the position of the midline in the left-right axis along the anteroposterior axis ("AP axis"), with the top and bottom of the diagrams pointing to the anterior and posterior directions respectively. Darker colors indicate that the midline is closer to the left side, while lighter colors indicate it is closer to the right side. Top diagram is the raw diagram, heavily affected by external vibration. The middle diagram is the result of filtering the top diagram to reduce the vibration artifacts. The bottom diagram shows the mid section of the filtered diagram, which is highly sensitive to the swinging contractions. The same diagram is shown in a time series representation in **(b)**.

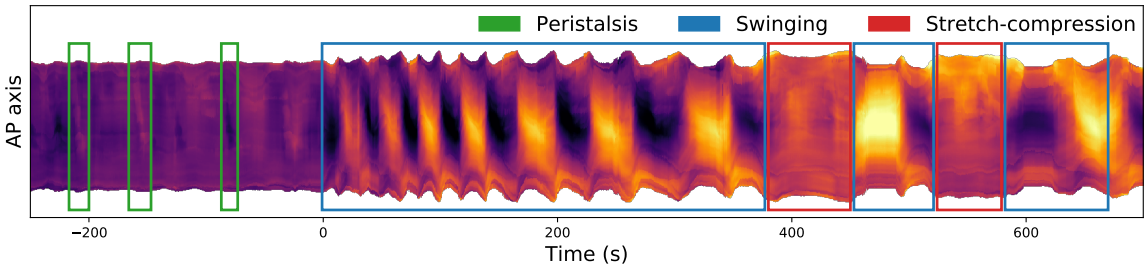

Figure 27. Behavior activity patterns example. Inset of the filtered time-space diagram of Figure 26a, showing the characteristic patterns generated by three different motor routines. The "AP axis" represents the anteroposterior axis. Same color scale as in Figure 26 was used.

I processed 6 videos of pupal behavior and generated the corresponding time-space diagrams (Figure 28a) and time series of the mid sections (Figure 28b). Since pupae were not stimulated with exogenous ETH at the beginning of the video was the case for calcium recordings, I aligned the diagrams and time series to the beginning of the ecdysis phase.

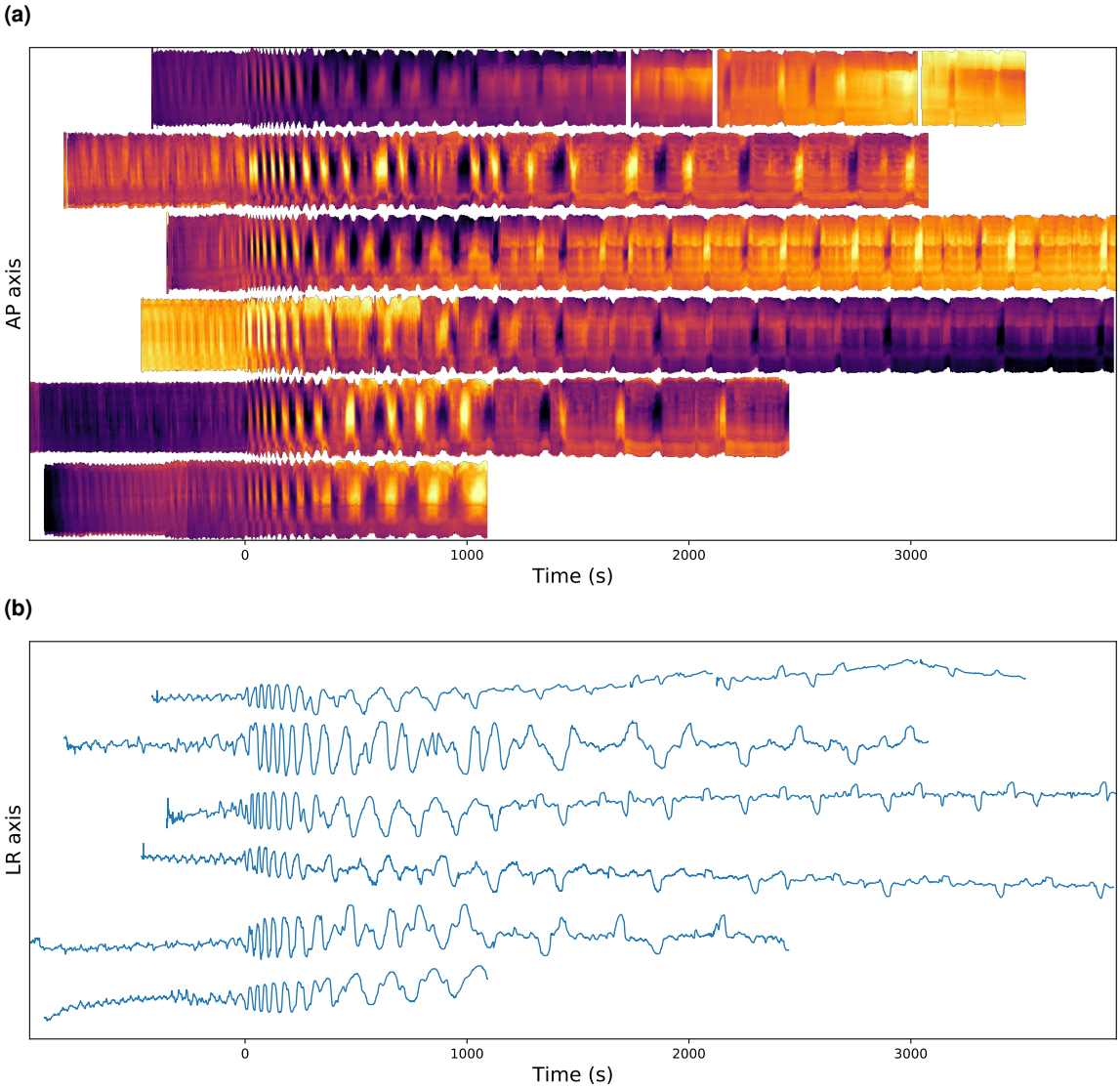

Figure 28. Behavior analyses. (a) filtered time-space diagrams of 6 pupal recordings aligned to the time where the ecdysis phase begins. White spaces in the top diagram were caused by the pupa getting out of the microscope viewing field as result of external vibration. **(b)** time series of the mid section of **(a)**. The "AP axis" and "LR axis" represent the anteroposterior and left-right axis respectively. Same color scale as in Figure 26 was used.

At first sight I noticed that all 6 time-space diagrams had a very similar pattern with very small differences in their timing and period. To see how the pupal behavior compares to the calcium activity I quantified the period of the motor patterns and the duration of the phases.

Quantifications were done manually by measuring time in the time-space diagram and time series plots (Figure 29, Table 18, 19, 20). In the pupal recordings, to measure the period I measured the duration of the largest time span of full cycles and divided it by the number of cycles. A swinging cycle was considered to be a bending to one side followed by a bending to the opposite side. During post-ecdysis a cycle includes the bending to both sides followed by the stretch-compression motor pattern. The quantification of the calcium imaging motor activity failed in some occasions to show alternating activity between the left and right regions, so I computed the period average from both regions.

The peristaltic contractions period of the pupa averaged 59.4 s (n = 6, SEM = 8.7 s). I was able to detect the motoneuron peristaltic activity in the motoneuronal recordings, but because of the low SNR and time resolution, apparently faster and more irregular activity, I was not able to quantify it reliably. I also noticed that the peristaltic activity tended to occur at the left and right regions simultaneously, suggesting that the motor routine is severely disrupted in the preparation.

The ecdysis swinging contraction period mean was 25.1 s (n = 9, SEM = 2.4 s) in the motoneuronal and 45.7 s (n = 6, SEM = 3.2 s) in the pupal recordings, showing significant differences between both groups (p-value < 0.002, two-tailed Mann-Whitney U test). The mean duration of the ecdysis phase was 346.7 s (n = 9, SEM = 37.8 s) for the motoneuronal recordings and 363.2 s (n = 6, SEM = 31.2 s) for the pupal recordings; these values were not significantly different.

The mean post-ecdysis cycle period was 128.8 s (n = 8, SEM = 37.0) in the motoneuronal recordings. In the pupal recordings, in contrast to the motoneuronal recordings, I noticed that the post-ecdysis phase could be divided into two subphases, a fast one followed by a slow one. Both subphases showed swinging alternated with stretch-compression contractions, but in the slower phase the stretch-compression tended to last longer. The mean period was 76.4 s (n = 6, SEM = 2.4) for the fast and 187.3 s (n = 5, SEM = 9.6 s) for the slow subphase. I compared the mean of the three groups and only found significant differences between the slow and fast post-ecdysis phase (p-value < 0.004, two-tailed Mann-Whitney U test). The mean duration of the fast post-ecdysis phase was 724.1 s (n = 5, SEM = 22.1). The slow post-ecdysis phase duration could not be measured as it persisted past the experimental recordings.

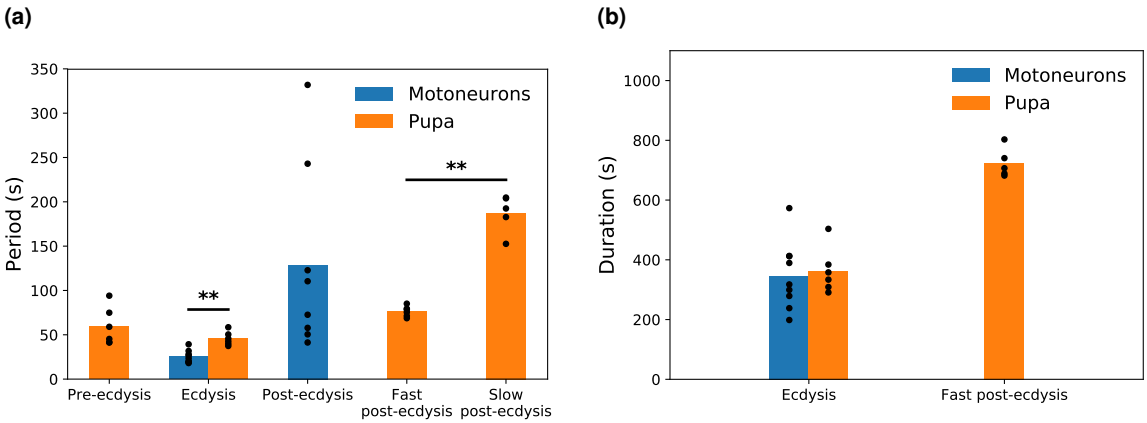

Figure 29. Behavior metrics. Metrics and comparison of the motoneuronal and pupal recording activity. **(a)** shows the period of the characteristic motor patterns of each ecdysis phases. **(b)** shows the duration of the ecdysis and fast post-ecdysis phase.

	Experiment										
	1	2	3	4	5	6	7	8	9	Mean	SEM
Ecdysis period (s)	19.6	18.9	31.8	20.0	39.3	23.4	18.1	28.0	26.5	25.1	2.4
Ecdysis duration (s)	412.0	279.0	573.0	299.4	413.1	198.5	389.5	238.2	317.6	346.7	37.8
Post-ecdysis period (s)	—	243.0	331.9	50.5	57.8	72.6	110.4	122.8	41.3	128.8	37.0

Table 18. Motoneuronal activity metrics. Values of Figure 29.

	Experiment							
	1	2	3	4	5	6	Mean	SEM
Pre-ecdysis period (s)	45.3	94.1	59.0	41.2	74.9	41.7	59.4	8.7
Ecdysis period (s)	42.6	58.5	37.4	39.8	50.4	45.7	45.7	3.2
Ecdysis duration (s)	358.0	503.6	333.7	290.8	384.1	309.0	363.2	31.2
Fast post-ecdysis period (s)	78.5	68.7	75.4	71.3	79.5	85.1	76.4	2.4
Slow post-ecdysis period (s)	203.9	204.8	152.6	182.8	192.5	—	187.3	9.6
Fast post-ecdysis duration (s)	688.8	706.7	802.9	682.0	740.3	—	724.1	22.1

Table 19. Pupal activity metrics. Values of Figure 29.

Groups		p-value
Motoneuronal ecdysis period	Pupal ecdysis period	0.001
Motoneuronal ecdysis duration	Pupal ecdysis duration	0.384
Motoneuronal post-ecdysis period	Pupal fast post-ecdysis period	0.298
Motoneuronal post-ecdysis period	Pupal slow post-ecdysis period	0.088
Pupal fast post-ecdysis period	Pupal slow post-ecdysis period	0.003

Table 20. Behavior metrics p-values. p-values of Figure 29.

I found that peristaltic waves are visible only during the pre-ecdysis phase, and have a shorter period in the pupal behavior recordings than in the motoneuronal recordings. The period of the swinging oscillations during the ecdysis phase were very close in both type of recordings. On the other hand, the swinging and stretch compression oscillation pairs lasted longer in the pupal behavior recording than in the motoneuronal recordings. I was not able to identify motoneuronal patterns that could be associated to the stretch compression motor pattern. I also found that the pupal oscillations during post-ecdysis were very regular in contrast to the motoneuronal oscillations.

In summary most of the activity observed in the pupal behavior recording has its fictive counterpart, but the motoneuronal recordings show different timing and higher irregularity, suggesting that sensory feedback could play an important role in the regulation of the ecdysis sequence.

4 Discussion

In this study I shed light on the dynamics of the peptidergic network that regulates the pupal ecdysis sequence in *Drosophila melanogaster*. In contrast to previous works, I took a more integrative approach by trying to link the calcium imaging recordings to the corresponding pupal ecdysis behavior. I used mathematical and computational tools to analyze the data, and this allowed me to discover more subtle features, hidden from less quantitative analyses.

In many occasions during the development of the thesis, decisions had to be made on what values or algorithms to use on a specific problem. Decisions were made considering the current knowledge of the underlying biology. In situations where the current knowledge did not provide enough detailed information, decisions were made based on the Occam's razor principle.

I found that CCAP neuron pairs showed different level of coupling depending on the pair. α CCAP neurons tightly regulate the motoneuronal activity during the ecdysis and post-ecdysis phase. The activity of CCAP neurons was highly variable across experiments, while the motoneuronal activity was more regular. I built a two-neuron model capable of reproducing the principal features of the motoneuronal activity. I discovered that the post-ecdysis phase can be divided into a fast and a slow oscillatory subphase, which were only visible in the pupal recordings. I also detected significant differences between the oscillation frequency of the ecdysis phase in the motoneuronal recordings and the pupal behavior recordings.

Based on the results obtained in the study, one possible model that could explain the results is described next. The ecdysis phase begins when CCAP neurons initiate their activity, which is similar between different CCAP neurons as result of their interconnectivity. CCAP neurons tightly regulate the motor activity during the ecdysis and post-ecdysis phase indirectly through a CPG. At high levels of activity, CCAP neurons generate swinging activity, while at low levels, stretch-compression activity. At some point during the post-ecdysis phase, CCAP neurons switch from a fast to a slow alternation between the swinging and stretch-compression motor programs. Sensory feedback keeps the activity tightly controlled in terms of oscillation frequency and regularity all the time.

4.1 CCAP neurons tightly regulate motoneuronal activity

CCAP neurons of the AN1-AN4 abdominal segments, have been identified as critical for the generation of the ecdysis motor patterns (Kim et al. 2006; Mena et al. 2016). How CCAP neurons are functionally coupled to the motor output was not clear, as there were no simultaneous recordings of CCAP neurons and motoneurons. Gammie and Truman 1997 showed in *Manduca sexta* that CCAP can turn on the ecdysial motor pattern, but it is not clear if this occurs in *Drosophila*.

The principal question I asked myself in the study was: How do CCAP neurons produce the motor output? Even though the question cannot be answered directly, I focused the study on characterizing the functional coupling of activity patterns. I began studying the activity of CCAP neurons and motoneurons from simultaneous recordings, kindly provided by Wilson Mena from John Ewer's laboratory.

The time series were analyzed in the time, frequency and time-frequency domains. The frequency and time-frequency domain transformations were done using CWT, a powerful mathematical tool that can decompose a signal into its frequency and phase components, while retaining the temporal dimension.

The oscillation frequency mismatch between α CCAP neurons and motoneurons pointed me to the existence of a CPG downstream the CCAP neurons. Through correlation analyses between CCAP neurons and the motoneuron amplitude at their primary oscillatory frequency, I found that the activity of both populations matched temporally. This temporal match persisted even after removing the pre-ecdysis phase from the analyses, showing that α CCAP neurons do not just trigger the initiation of the ecdysis phase, but tightly regulate motoneuronal activity during the complete ecdysis sequence.

What might be the advantage of having CCAP neurons that modulate the CPG continuously and not just initiate its activity ballistically? One possible answer could be that, in this way the behavior can be controlled not just by direct regulation of the CPG, but also indirectly via CCAP neurons, which increase the flexibility of the system. As it has been shown in previous studies (Mena et al. 2016), γ-aminobutyric acid (GABA) affects the activity of AN1-AN4 CCAP neurons, in this way GABAergic neurons could regulate the motoneuron oscillatory activity indirectly. This could be the mechanism behind the inhibition of these motoneurons during the stretch-compression phase, as they appear to be involved in the swinging motor behavior only.

During the writing of the thesis, a related paper was published by Diao et al. 2017. They identified populations of neurons that express the receptor of Bursicon and display oscillatory activity similar to the activity of the motoneurons. They suggested that these neurons are part of the CPG that regulates

the motoneuronal activity, which they found expressed CCAP receptor (CCAP-R). They also showed that through the activation and inactivation of AN1-AN4 CCAP neurons, they were able to initiate the ecdysis phase or completely suppress it respectively. The tight coupling I found between CCAP neurons and motoneurons agrees with these findings, as they showed experimentally that CPG neurons and motoneurons are direct peptidergic target of CCAP neurons.

4.2 CCAP neurons and motoneurons form a degenerate and robust system

To better understand the relationship between α CCAP neurons and motoneurons, I built an abstract logistic model that takes the activity of the α CCAP neurons as input and computes the motoneuronal oscillatory activity as output.

The logistic model computes the probability that motoneurons oscillate at any given time. The model showed that α CCAP neurons are good predictors of the motoneuronal oscillatory state, being able to predict the motoneuronal oscillatory state with an error rate $<10\,\%$, which shows how tightly coupled these two neuron populations are.

I found that the fitting of the model to different experiments required in average 4 neurons of a total of 8, which appears to have been mainly caused by the redundant activity of the α neurons. That, in addition to the high variability of the weights across the experiments, suggests that the system is degenerate, or in other words, can produce the same solution from different configurations (Edelman and Gally 2001; Whitacre 2010). Through the multiplicity of the neurons and their signals, the system becomes more robust against failure, as it has functional redundancy. This could explain why some α CCAP neurons with completely abnormal activity would not cause any noticeable abnormal effect in the motoneuronal activity pattern. This degeneracy is described in detail in the review of Edelman and Gally 2001 where they show examples on how it occurs at all levels of biological organization. For instance, at the level of genetic code, different nucleotide sequences can encode the same amino acid sequence. At the cellular level, no individual cell within a tissue is indispensable. At the level of body movements, same movement can be generated through different patterns of muscle contraction.

4.3 A two-neuron conductance-based model can reproduce all the major features of the motoneuronal pattern of activity

As the logistic model is incapable of modeling the calcium dynamics, I built one that could. As numerous authors have already described (Hooper 2000; Marder and Bucher 2001; Selverston 2010), there are multiple CPG circuit topologies that can generate rhythmic activity; and in the absence of a circuit description, I arbitrarily chose a simple model that could be adjusted to the experimental data.

I took as a starting point a CPG model developed by Jalil et al. 2010, which is a two reciprocally inhibiting endogenously bursting neuron model with antiphase synchronization. I added equations to add an α CCAP neuron input, current noise, and fluorescence (calcium) dynamics.

The model was adjusted to match the oscillation timing, the period, the duty cycle, the phase noise, and the time constant to the experimental data. The adjusted models showed a good match in all the features I tried to adjust the parameters to, and revealed how the different parameters affect the model dynamics.

The reason I used two neurons to model a population of left and right neurons, is that the neurons of each side appear to have identical activity with a slightly increasing phase lag along the axis (which could not be measured reliably at the time resolution of the recording). In the case a model with such motoneuronal activity is desirable, Gjorgjieva et al. 2013 showed one way to achieve that, by using a network of interconnected Wilson-Cowan units along the anteroposterior axis, where the signal lags each time it travels to a different unit. Other, probably more interesting ways to extend the model could include the addition of sensory feedback (Marder and Bucher 2001), or the addition of a stretch-compression circuit.

In contrast to well-studied peptidergic networks such as the crustacean stomatogastric nervous system (Marder and Bucher 2007; Stein 2009), very little is known about the neuronal architecture that underlies the ecdysis behavioral sequence. I proposed a modeling framework that captures all the major features of the motoneuronal activity and may work as a stepping stone for the development of more complex models as more details about the underlying circuit are discovered.

4.4 Sensory feedback may play an important role in the behavior regulation

I developed an algorithm that robustly detects the pupal midline, which I then used to generate a time-space diagram. The diagram showed distinctive patterns for all major motor patterns and was used to quantify the pupal activity. The quantification was made in terms of period and duration of the different pupal activity patterns and was then compared to the motoneuronal activity.

The calcium imaging and puparium-free preparations showed characteristic activity patterns in each of the ecdysis phases, but with important differences in their timing. The calcium imaging preparation appeared to have more irregular and shorter cycles during pre-ecdysis and ecdysis than the puparium-free preparation. Additionally, I found that the post-ecdysis phase could be divided into two subphases, a fast and a slow subphase, which appeared to be absent in the calcium imaging preparation.

These differences could be the result of multiple factors, as both preparations differ considerably. One possibility is that they are the result of the disruption of the sensory feedback, which has been shown to be critical for the proper regulation of the motor behavior in many animals (Ayali et al. 2015; Büschges et al. 2008; Hughes and Thomas 2007). The puparium-free preparation may also display different motoneuronal behavior than the intact puparium preparation, as the sensory feedback differs in both cases.

Nonetheless the puparium-free preparations give us hints on what kind of activity to expect from the recorded neurons, and may help us theorize on how feedback affects the behavioral sequence.

4.5 Future projections

In my study I only used wild type flies, but the analysis of genetically or pharmacologically manipulated animals with the developed tools should be trivial, and could uncover new insights on the behavioral sequence.

In the future, there are number of avenues that may be explored and could lead to a better understanding of the regulatory mechanisms behind the ecdysis sequence. As CCAP neurons appear to be tightly coupled to the motoneuronal activity during the ecdysis and post-ecdysis phases, it is possible that these neurons regulate the motor activity by selecting what motor program the CPG executes. It will be interesting to see if the experimental activation and inactivation of CCAP neurons would allow researchers to control the alternation between the swinging and stretch-compression motor programs. Another important question that will be relevant to answer is, how is the activity of the CCAP neurons regulated? Is the oscillatory activity intrinsic? How is the switching between the CCAP neuron activity

patterns regulated? It also will be interesting to see what new discoveries, in the connectivity and dynamics of the CPG neurons found by Diao et al. 2017, will follow and lead to a better understanding of the dynamics of the CPG. Finally, ETHR-B neurons appear to play an important role during the pre-ecdysis phase (Diao et al. 2017; Mena et al. 2016) and their study will be required if we truly want to understand the structure and dynamics that underlie the ecdysis behavior.

5 Conclusions

The main conclusions of the thesis can be summed up as follows:

- CCAP neurons are all coordinated.
- α and β CCAP neurons are highly coupled to contralateral neurons.
- β CCAP neurons are also highly coupled to their ipsilateral counterparts.
- Left and right motoneurons oscillate at a 180° phase difference with relevant phase noise.
- The activity of CCAP neurons is highly variable across experiments, while the motoneuronal activity is more regular.
- α CCAP neurons are highly coupled to the motoneuronal activity.
- An abstract logistic model can predict the oscillation probability with high accuracy.
- On average only 4 neurons are needed to predict the oscillation probability with the highest accuracy, as the signals are highly redundant.
- A two-neuron conductance-based model can simulate many of the activity pattern features observed in the experimental recordings and servers as a framework to study the oscillatory activity.
- Puparium free preparations display a fast and a slow oscillatory post-ecdysis subphase, not visible in the motoneuronal recordings.
- There are significant differences between the oscillation frequency of the ecdysis phase in the motoneuronal recordings and the pupal behavior recordings.

References

Akaike, H. (1974). “A new look at the statistical model identification”. In: *IEEE Transactions on Automatic Control* 19.6, pp. 716–723.

Anderson, D. J. and Perona, P. (2014). “Toward a Science of Computational Ethology”. In: *Neuron* 84.1, pp. 18–31.

Arakane, Y., Li, B., Muthukrishnan, S., Beeman, R. W., Kramer, K. J., and Park, Y. (2008). “Functional analysis of four neuropeptides, EH, ETH, CCAP and bursicon, and their receptors in adult ecdysis behavior of the red flour beetle, Tribolium castaneum”. In: *Mechanisms of Development* 125, pp. 984–995.

Ayali, A., Couzin-Fuchs, E., David, I., Gal, O., Holmes, P., and Knebel, D. (2015). “Sensory feedback in cockroach locomotion: current knowledge and open questions”. In: *Journal of Comparative Physiology A: Neuroethology, Sensory, Neural, and Behavioral Physiology* 201.9, pp. 841–850.

Baker, J. D., McNabb, S. L., and Truman, J. W. (1999). “The hormonal coordination of behavior and physiology at adult ecdysis in Drosophila melanogaster.” In: *The Journal of Experimental Biology* 202.Pt 21, pp. 3037–3048.

Bargmann, C. I. (2012). “Beyond the connectome: How neuromodulators shape neural circuits”. In: *BioEssays*.

Brezina, V. (2010). “Beyond the wiring diagram: signalling through complex neuromodulator networks.” In: *Philosophical transactions of the Royal Society of London. Series B, Biological sciences* 365.1551, pp. 2363–74.

Büschges, A., Akay, T., Gabriel, J. P., and Schmidt, J. (2008). “Organizing network action for locomotion: Insights from studying insect walking”. In: *Brain Research Reviews* 57.1, pp. 162–171.

Carlson and Bentley, D. (1977). “Ecdysis: neural orchestration of a complex behavioral performance”. In: *Science* 195.4282, pp. 1006–1008.

Darwin, C. (1859). *On the Origin of Species, 1859*. New York : Routledge.

Delcomyn, F. (1980). “Neural basis of rhythmic behavior in animals”. In: *Science* 210.4469, pp. 492–498.

Diao, F., Elliott, A. D., Diao, F., Shah, S., and White, B. H. (2017). “Neuromodulatory connectivity defines the structure of a behavioral neural network”. In: *eLife* 6.1984, pp. 1–30.

Diao, F., Mena, W., Shi, J., Park, D., Diao, F., Taghert, P., Ewer, J., and White, B. H. (2016). “The splice isoforms of the Drosophila ecdysis triggering hormone receptor have developmentally distinct roles”. In: *Genetics* 202.1, pp. 175–189.

Dickinson, P. S. (2006). “Neuromodulation of central pattern generators in invertebrates and vertebrates”. In: *Current Opinion in Neurobiology* 16.6, pp. 604–614.

Edelman, G. M. and Gally, J. a. (2001). “Degeneracy and complexity in biological systems.” In: *Proceedings of the National Academy of Sciences of the United States of America* 98.24, pp. 13763–8.

Ewer, J., Gammie, S. C., and Truman, J. W. (1997). “Control of insect ecdysis by a positive-feedback endocrine system: roles of eclosion hormone and ecdysis triggering hormone.” In: *The Journal of experimental biology* 200, pp. 869–81.

Gammie, S. C. and Truman, J. W. (1997). “Neuropeptide hierarchies and the activation of sequential motor behaviors in the hawkmoth, Manduca sexta”. In: *The Journal of neuroscience : the official journal of the Society for Neuroscience* 17.11, pp. 4389–4397.

Gjorgjieva, J., Berni, J., Evers, J. F., and Eglen, S. J. (2013). “Neural circuits for peristaltic wave propagation in crawling Drosophila larvae: analysis and modeling”. In: *Frontiers in Computational Neuroscience* 7.April, pp. 1–19.

Gomez-Marin, A., Paton, J. J., Kampff, A. R., Costa, R. M., and Mainen, Z. F. (2014). “Big behavioral data: Psychology, ethology and the foundations of neuroscience”. In: *Nature Neuroscience* 17.11, pp. 1455–1462.

Griffith, L. C. (2012). “Identifying behavioral circuits in Drosophila melanogaster: moving targets in a flying insect.” In: *Current opinion in neurobiology* 22.4, pp. 609–14.

Hooper, S. (2000). “Central pattern generators”. In: *Current biology : CB* 10.5, R176.

Hughes, C. L. and Thomas, J. B. (2007). “A sensory feedback circuit coordinates muscle activity in Drosophila”. In: *Molecular and Cellular Neuroscience* 35.2, pp. 383–396.

Hya, A., Giraud, A.-l., Fontolan, L., and Gutkin, B. (2015). “Neural Cross-Frequency Coupling : Connecting Architectures , Mechanisms , and Functions”. In: *Trends in Neurosciences* 38.11, pp. 725–740.

Jalil, S., Belykh, I., and Shilnikov, A. (2010). “Fast reciprocal inhibition can synchronize bursting neurons”. In: *Physical Review E - Statistical, Nonlinear, and Soft Matter Physics* 81.4, pp. 1–4.

Karsai, G., Pollák, E., Wacker, M., Vömel, M., Selcho, M., Berta, G., Nachman, R. J., Isaac, R. E., Molnár, L., and Wegener, C. (2013). “Diverse in- and output polarities and high complexity of local synaptic and non-synaptic signaling within a chemically defined class of peptidergic Drosophila neurons”. In: *Frontiers in Neural Circuits* 7.August, pp. 1–22.

Kazama, H. (2015). “Systems neuroscience in Drosophila: Conceptual and technical advantages”. In: *Neuroscience* 296, pp. 3–14.

Kim, D.-H., Han, M.-R., Lee, G., Lee, S. S., Kim, Y.-J., and Adams, M. E. (2015). “Rescheduling Behavioral Subunits of a Fixed Action Pattern by Genetic Manipulation of Peptidergic Signaling”. In: *PLOS Genetics* 11.9. Ed. by Schoofs, L.

Kim, Y.-J., Zitnan, D., Galizia, C. G., Cho, K.-H., and Adams, M. E. (2006). “A command chemical triggers an innate behavior by sequential activation of multiple peptidergic ensembles.” In: *Current biology : CB* 16.14, pp. 1395–407.

Kingan, T. G., Gray, W., Zitnan, D., and Adams, M. E. (1997). “Regulation of ecdysis-triggering hormone release by eclosion hormone.” In: *The Journal of experimental biology* 200.Pt 24, pp. 3245–3256.

Lahr, E. C., Dean, D., and Ewer, J. (2012). “Genetic analysis of ecdysis behavior in Drosophila reveals partially overlapping functions of two unrelated neuropeptides.” In: *The Journal of neuroscience : the official journal of the Society for Neuroscience* 32.20, pp. 6819–29.

Levitis, D. A., Lidicker, W. Z., and Freund, G. (2009). “Behavioural biologists do not agree on what constitutes behaviour”. In: *Animal Behaviour* 78.1, pp. 103–110.

Li, K. (2008). *The image stabilizer plugin for ImageJ*.

Loveall, B. J. and Deitcher, D. L. (2010). “The essential role of bursicon during drosophila development”. In: *BMC Developmental Biology* 10.

Marder, E. and Bucher, D. (2001). “Central pattern generators and the control of rhythmic movements.” In: *Current biology : CB* 11.23, R986–96.

Marder, E. and Calabrese, R. L. (1996). “Principles of rhythmic motor pattern generation.” In: *Physiological reviews* 76.3, pp. 687–717.

Marder, E. (2011). “Variability, compensation, and modulation in neurons and circuits.” In: *Proceedings of the National Academy of Sciences of the United States of America* 108 Suppl, pp. 15542–8.

— (2012). “Neuromodulation of neuronal circuits: back to the future.” In: *Neuron* 76.1, pp. 1–11.

Marder, E. and Bucher, D. (2007). “Understanding Circuit Dynamics Using the Stomatogastric Nervous System of Lobsters and Crabs”. In: *Annual Review of Physiology* 69.1, pp. 291–316.

Mena, W., Diegelmann, S., Wegener, C., and Ewer, J. (2016). “Stereotyped responses of Drosophila peptidergic neuronal ensemble depend on downstream neuromodulators.” In: *eLife* 5, p. 22.

Nässel, D. R. and Winther, A. M. E. (2010). “Drosophila neuropeptides in regulation of physiology and behavior.” In: *Progress in neurobiology* 92.1, pp. 42–104.

Nusbaum, M. P. and Blitz, D. M. (2012). “Neuropeptide modulation of microcircuits.” In: *Current opinion in neurobiology* 22.4, pp. 592–601.

Park, J. H., Schroeder, A. J., Helfrich-Förster, C., Jackson, F. R., and Ewer, J. (2003). “Targeted ablation of CCAP neuropeptide-containing neurons of Drosophila causes specific defects in execution and circadian timing of ecdysis behavior”. In: *Development* 130.12, pp. 2645–2656.

Park, Y., Filippov, V., Gill, S. S., and Adams, M. E. (2002). “Deletion of the ecdysis-triggering hormone gene leads to lethal ecdysis deficiency.” In: *Development (Cambridge, England)* 129.2, pp. 493–503.

Rasband, W. (2013). *ImageJ*.

Reynolds, S. E. (1980). “Integration of Behaviour and Physiology in Ecdysis”. In: *Advances in Insect Physiology* 15.C, pp. 475–595.

Santos, J. G., Vömel, M., Struck, R., Homberg, U., Nässel, D. R., and Wegener, C. (2007). “Neuroarchitecture of peptidergic systems in the larval ventral ganglion of Drosophila melanogaster.” In: *PloS one* 2.8, e695.

Selverston, A. I. (2010). “Invertebrate central pattern generator circuits.” In: *Philosophical transactions of the Royal Society of London. Series B, Biological sciences* 365.1551, pp. 2329–45.

Shilnikov, A. and Cymbalyuk, G. (2005). “Transition between tonic spiking and bursting in a neuron model via the blue-sky catastrophe.” In: *Physical review letters* 94.4, p. 048101.

Stein, W. (2009). “Modulation of stomatogastric rhythms”. In: *Journal of Comparative Physiology A: Neuroethology, Sensory, Neural, and Behavioral Physiology* 195.11, pp. 989–1009.

Whitacre, J. M. (2010). “Degeneracy: a link between evolvability, robustness and complexity in biological systems.” In: *Theoretical biology & medical modelling* 7, p. 6.

Whitacre, J. and Bender, A. (2010). “Degeneracy: a design principle for achieving robustness and evolvability.” In: *Journal of theoretical biology* 263.1, pp. 143–53.

Zhang, X., Leng, G., and Feng, J. (2010). “Coherent peptide-mediated activity in a neuronal network controlled by subcellular signaling pathway: experiments and modeling.” In: *Journal of biotechnology* 149.3, pp. 215–25.

Zilkha, N., Sofer, Y., Beny, Y., and Kimchi, T. (2016). “From classic ethology to modern neuroethology: Overcoming the three biases in social behavior research”. In: *Current Opinion in Neurobiology* 38, pp. 96–108.

Zitnan, D. (2003). “Conservation of ecdysis-triggering hormone signalling in insects”. In: *Journal of Experimental Biology* 206.8, pp. 1275–1289.

Zupanc, G. (2010). “Neuroethology”. In: *Scholarpedia* 5.10, p. 5306.